Journal of Geophysical Research: Planets

RESEARCH ARTICLE
10.1029/2017JE005461

Key Points:
- Diverse hydrous minerals are mapped in Amazonian-aged Lyot crater with prehnite detections on the crater rim
- Hydrous minerals are not found associated with the fluvial channels emanating from Lyot's ejecta blanket
- Localized channel-forming events occurred in the Amazonian, when there may have been ground ice, but mineralization was limited or absent

Correspondence to:
L. Pan,
lu.pan@univ-lyon1.fr

Citation:
Pan, L., & Ehlmann, B. L. (2018). Aqueous processes from diverse hydrous minerals in the vicinity of Amazonian-aged Lyot crater. *Journal of Geophysical Research: Planets*, *123*, 1618–1648. https://doi.org/10.1029/2017JE005461

Received 9 OCT 2017
Accepted 24 MAY 2018
Accepted article online 31 MAY 2018
Published online 10 JUL 2018

Aqueous Processes From Diverse Hydrous Minerals in the Vicinity of Amazonian-Aged Lyot Crater

Lu Pan[1,2] **and Bethany L. Ehlmann**[1,3]

[1]California Institute of Technology, Division of Geological and Planetary Sciences, Pasadena, CA, USA, [2]Université Claude Bernard Lyon 1, Now at Laboratoire de Geologie de Lyon, Villeurbanne, France, [3]California Institute of Technology, Jet Propulsion Laboratory, Pasadena, CA, USA

Abstract Amazonian-aged Lyot crater is the best-preserved and deepest peak-ring impact crater (diameter, D = 220 km) in the northern lowlands of Mars. Morphological features including scouring channels emanating from its ejecta and small channels within the crater have been examined previously to understand hydrological activity associated with the crater. In this study, we analyze images acquired by the Compact Reconnaissance Imaging Spectrometer for Mars on board the Mars Reconnaissance Orbiter to investigate the mineralogical record in Lyot and its surroundings, which are presently enriched in ground ice, to understand the associated aqueous processes, their relative timing, and a possible role for ground ice in hydrous mineral formation. We find diverse hydrous minerals, including Fe/Mg phyllosilicates, chlorite, illite/muscovite, and prehnite in Lyot crater walls, central peak, and ejecta, as well as in two craters to the west of Lyot. The exposure and distribution of the hydrous minerals suggest that they are related to the impact process, either exposed by the excavation of hydrothermally altered rocks or formed through syn-depositional hydrothermal alteration immediately after impacts. The Lyot impact induced channel formation to the north, but no mineralogical evidence of aqueous alteration associated with the channels is observed. The sinuous channels within Lyot, diverted by bedrock units with hydrous mineral detections, did not cause mineralization but likely represent the last stage of water activity in Lyot crater. The separate episodes of water activity indicate flow of liquid water on Mars' surface during the Amazonian but limited to no aqueous alteration to generate hydrous minerals.

Plain Language Summary Though liquid water is not stable on the surface of Mars presently, water may have had a more active role on Mars in the recent geologic epoch. In particular, meteor impacts may melt ground ice, creating local environments with liquid water activity. Lyot crater is the deepest, well-preserved impact crater in the northern plains of Mars, with a diameter of 220 km, formed in the most recent geologic epoch. In this work, we study the mineralogy and morphology related to water activities within and adjacent to Lyot crater. One of the mineral types (prehnite) found in Lyot form at relatively high temperature (>200 °C) in hydrothermal environments. From the distribution of water-bearing minerals, we found that they probably represent an earlier episode of water activity before or during the impact. While liquid water has carved small channels inside the crater long after the impact, they probably did not exist on the surface long enough to alter the composition of the bedrock materials. Liquid water may be present but probably quite short-lived in the most recent epoch on Mars.

1. Introduction

Mars throughout the Amazonian period is thought to be similar to present day Mars—relatively cold and dry with few indications of surface liquid water activity—as opposed to the Noachian and Hesperian periods, which are characterized by the formation of valley networks and large outflow channels. The widespread hydrous mineral detections made by instruments like the Observatoire pour la Minéralogie, l'Eau, les Glaces et l'Activité on board Mars Express and the Compact Reconnaissance Imaging Spectrometer for Mars (CRISM) on board the Mars Reconnaissance Orbiter (MRO) are also found mostly in Noachian- and Hesperian-aged terrains, while the youngest surfaces on Mars lack hydrous mineral detections at orbital scale (Bibring et al., 2006; Carter et al., 2013; Ehlmann & Edwards, 2014; Mustard et al., 2008). Together, these data suggest that by the start of Amazonian period, the widespread, global hydrological activity characteristic of early Mars had transitioned to a cold and arid environment where water changes phase directly from ice to vapor with few occurrences of liquid water. However, emerging evidence from orbital observations suggests that Amazonian Mars is more active than previously thought. The variety of active geologic processes

includes formation of small valley and channel systems (Dickson et al., 2009; Fassett et al., 2010), widespread mantling units in the midlatitudes of Mars (Head et al., 2003; Mustard et al., 2001), formation of gullies on crater central peaks and walls (Malin & Edgett, 2000; Mellon & Phillips, 2001), and the activity of recurring slope lineae (McEwen et al., 2011; Ojha et al., 2015). Understanding the forms of potentially water-related activity in the Amazonian is crucial to our understanding of the changing hydrological cycle and climate on Mars.

Modern day subsurface midlatitude and high-latitude ice is observed in fresh impact craters (Byrne et al., 2009) and as slabs on select scarps (Dundas et al., 2018). A global cryosphere with ice stable in the subsurface in the middle to high latitudes has been predicted in the Amazonian (Clifford, 1993; Clifford & Parker, 2001) and is supported by features that are interpreted as glacial in origin, such as lobate debris apron, linear valley fill, and concentric crater fill (Dickson et al., 2008; Head et al., 2006; Levy et al., 2007, 2010; Lucchitta & Earth, 1981; Squyres, 1978). During this period, impact cratering and volcanism may have been important in shaping the global climate and may have created localized habitable environments on the surface of Mars. The vaporization of water ice or the melting and circulation of groundwater in the subsurface by impacts are thus one possible form of aqueous activity in the Amazonian (Abramov & Kring, 2005; Barnhart et al., 2010; Rathbun & Squyres, 2002).

Lyot crater is the deepest well-preserved impact peak-ring crater in the northern lowlands of Mars, with a diameter of 220 km. The impact event is dated to be Early Amazonian, after the cessation of ancient valley network activity (Dickson et al., 2009). As the youngest large impact in the northern lowlands, located near the dichotomy boundary and close to Deuteronilus Mensae where subsurface ice has been detected (Baker & Carter, 2017; Plaut et al., 2009, 2010), the impact event could have interacted with the local cryosphere and induced significant effects on the global climate in the Amazonian. The Lyot impact is similar in size to the Chicxulub crater (with its collapsed transient cavity diameter of ~150 km and a maximum damage diameter of ~250 km; J. V. Morgan et al., 2000) on Earth, impacted at the Cretaceous-Tertiary (K-T) boundary (Renne, 2013). Such energetic impacts can cause a series of effects on climate, including the release of subsurface CO_2 and H_2O into atmosphere; dust and aerosol loading; and a localized hydrothermal or groundwater system (Abramov & Kring, 2005; Segura et al., 2008, 2012; Toon et al., 2010). Fluvial landforms may form in such systems via various mechanisms, including channels emanating from ejecta blankets (Jones et al., 2011; G. A. Morgan & Head, 2009), small valleys from groundwater sapping (Brakenridge et al., 1985) or channels on crater terraces and rims from impact-generated precipitation (McEwen, Hansen, et al., 2007). These processes with liquid water may result in the formation of secondary minerals due to hydrothermal alteration in the impact melt sheet or impacted bedrock, as suggested to occur in terrestrial craters and could be important for Mars (Allen et al., 1982; Newsom, 1980; Osinski et al., 2013; Tornabene et al., 2013). This impact-induced mechanism for the formation of hydrous minerals on Mars is supported by theoretical modeling work (Barnhart et al., 2010; Rathbun & Squyres, 2002; Schwenzer & Kring, 2009) and has been invoked to explain the observed mineralogy in Majuro crater (Mangold et al., 2012) and Toro crater (Marzo et al., 2009). In addition to generation of an impact hydrothermal system, large impacts may also be relevant to the aqueous alteration of primary minerals through devitrification, autometamorphism, and preferred alteration of damaged materials (Tornabene et al., 2013).

The vicinity of Lyot crater has been found with spectral signatures consistent with spatially concentrated exposures of diverse hydrous minerals relative to the entire northern lowlands (Pan et al., 2017), including phases in addition to chlorite-prehnite detections mapped by Carter et al. (2010). Here we specifically investigate the spatial distribution of these hydrous minerals and relationships with previously identified water-related surface features in the vicinity of Lyot, examining whether their origins are related. In particular, while most other large craters on Mars appear to have mostly hydrous minerals excavated from the subsurface (Carter et al., 2013; Ehlmann et al., 2011), we consider whether in Lyot the postimpact fluvial activity might be related to mineralization. The ice-rich nature of this region makes it a prime location for impact-related heating to develop mineralized deposits.

2. Geological Context of Lyot and Previous Work

Located close to the dichotomy boundary in the northern lowlands of Mars, Lyot crater (50.46°N, 29.31°E) is a peak ring crater with both a central peak and a peak ring structure. To the south of Lyot is the chaos terrain of Deuteronilus Mensae, a region of dissected valleys, mesas, knobs, and craters of various origin and age

(Lucchitta, 1984; Parker et al., 1989). Linear valley fills and lobate apron deposits have been found to be widespread in this region and are hypothesized to be related to Amazonian glacial deposits (Baker et al., 2010; Dickson et al., 2008; Head et al., 2006; G. A. Morgan et al., 2009). Using Mars SHAllow RADar (SHARAD) sounder radargrams, extensive subsurface ice deposits have been detected in the Deuteronilus Mensae region and are correlated with surface morphology features, including lobate debris aprons and linear valley fills (Plaut et al., 2009, 2010). To the east of the region, a recent survey using SHARAD data showed that the regionally extensive, younger mantling units are also subsurface ice-rich deposits (Baker & Carter, 2017).

The crustal structure near Lyot is likely similar to that of the rest of the northern lowlands (Frey, 2002; Russell & Head, 2002) with older Noachian terrains, ~1-km-thick overlying Hesperian lava flows, and Amazonian surface materials. Based on the relationship with adjacent units (including crater ejecta overlying Hesperian ridged plains and the mantling materials inside craters; Russell & Head, 2002) and crater count statistics (Dickson et al., 2009), the Lyot impact is inferred to have occurred in the Early Amazonian epoch (Figure 1b).

Previous studies have focused on the morphological features near Lyot crater and the indications of water activity at different points in time. Initial attempts to identify features related to surface water (Russell & Head, 2002) in Viking, Mars Orbiter Laser Altimeter (MOLA), and Mars Orbiter Camera data did not find channels, valleys, crater wall gullies, crater floor sedimentation, or layered deposits. Later investigations of higher resolution imagery from the Context Camera (CTX; Malin et al., 2007) on board MRO and the Thermal Emission Imaging System (THEMIS; Christensen et al., 2004) on board the Mars Odyssey identified water-related features within and outside of Lyot: Extensive fluvial channels are found to the north of Lyot, emanating from the margin of its ejecta blanket (Harrison et al., 2010). Similar channels emanating from ejecta (and/or dissected terrains) were observed associated with well-preserved large craters on Noachian terrains, (G. A. Morgan & Head, 2009; Jones et al., 2011). Proposed formation mechanisms for channels emanating from ejecta blankets include dewatering of hot impact ejecta (Harrison et al., 2010; Jones et al., 2011; G. A. Morgan & Head, 2009; Weiss et al., 2017), seismically triggered shallow groundwater flow (Harrison et al., 2010), or melting of surface snow/ice (Weiss et al., 2017). Within Lyot crater, kilometer-long fluvial channels emanate from crater walls, possibly due to localized melting of ice, promoted by the relatively higher surface atmospheric pressures, which result from the low elevation of crater floor (Dickson et al., 2009). Through these fluvial processes during or after the impact, mineralization may be expected to be spatially correlated with the fluvial morphology. In general, impact-generated fluvial processes may also induce higher level of alteration within the crater central region, although impact melt deposition may also result in alteration on the ejecta for large complex craters (Naumov, 2005; Osinski, 2005; Osinski et al., 2013; Tornabene et al., 2013). Here we combine analysis of mineralogy with geomorphology to better distinguish these scenarios and provide new constraints on the formation environment of Lyot's hydrous minerals and the aqueous processes that occurred.

3. Methods

3.1. Impact Craters Selection

Five craters (Lyot; Micoud; and the unnamed craters c308, c375, and c194) were selected for mineralogy analysis and mapping, based on initial reconnaissance to locate hydrous minerals (Pan et al., 2017) with CRISM data of all craters $>$1 km in the Lyot vicinity. The c### designation corresponds to the crater ID of unnamed craters in the Mars global crater database (Robbins & Hynek, 2012a).

3.2. Mineral Identification and Mapping Using CRISM Data

To identify and map the different hydrous minerals in the Lyot vicinity, we studied the full and half resolution targeted images (with resolution 18–36 m/pixel) from CRISM on board MRO. CRISM is a push-broom imaging spectrometer, which acquires visible/shortwave-infrared wavelength reflectance data over two detectors between 0.36 and 3.92 μm with the highest spatial resolution of 15–19 m/pixel (Murchie et al., 2007). Data processing follows standard routines (e.g., Ehlmann et al., 2009; Murchie et al., 2009), including converting radiance to I/F data, photometric correction, and atmospheric correction based on the volcano scan method (Murchie et al., 2007). After converting to I/F data, we apply a denoising algorithm (method details in Pan et al., 2017). In brief, we first remove statistical outliers in the spectral domain. We then calculate column-specific "bland" spectra to use as denominators, by using the median of pixels in the same column that

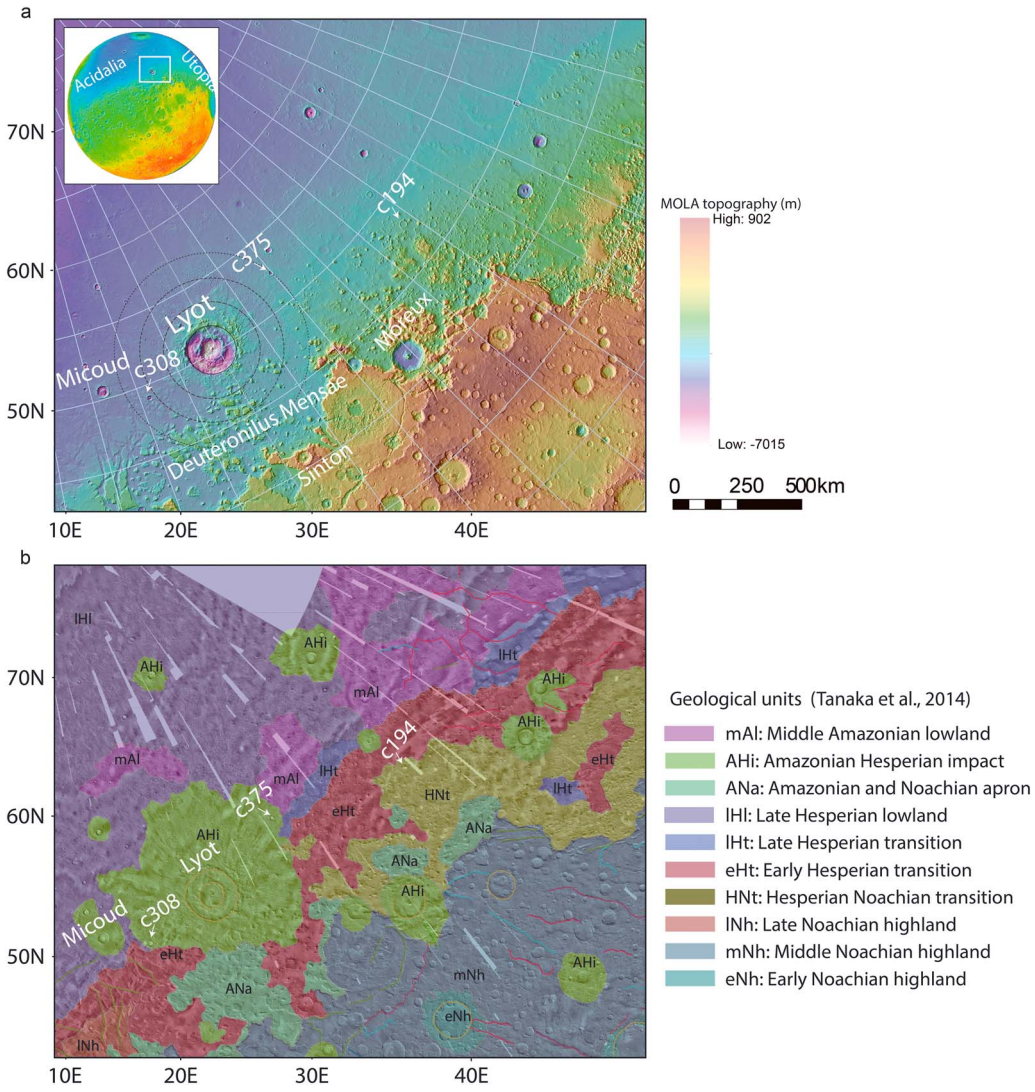

Figure 1. The geologic context of the study region of Lyot crater and its vicinity near the dichotomy boundary: (a) Lyot crater at 55°N, 30°E, and four craters (Micoud, c308, c375, and c194) in the vicinity of Lyot investigated in this study on Mars topography map from Mars Orbital Laser Altimeter, in Mars North Polar Stereographic Projection; (b) geological units mapping of the same region (Tanaka et al., 2014). Amazonian units are in green, and Hesperian units are in red and purple. Except for c194, which is situated in the Hesperian-Noachian transition unit, all the other craters investigated in this study are mapped as Amazonian-Hesperian impacts (AHi), overlying the late Hesperian terrains of the northern lowlands.

lack absorptions in mineral parameter maps. By ratioing the original spectrum of each pixel to the spectrally bland spectra, we compute a ratioed image cube, which is then used for identifying mineralogy. We perform spectral parameter analysis where we highlight pixels with strengthened absorptions at specific wavelengths for easy identification of spectrally interesting regions, using customized spectral parameters (Table 1). We verify the denoising algorithm products by comparison to products based on standard parameter maps (Pelkey et al., 2007).

We analyzed 73 CRISM-targeted images covering the impact structures of the five craters with previously identified mafic and/or hydrous minerals; 32 images covering the overland channels to the north of Lyot; and 93 images covering the ice-rich regions of Deuteronilus Mensae. Using the ratioed infrared spectral data, we identify different spectral classes, based on consistent band location and width and covarying depths. Different spectral classes identified in CRISM images are compared with the U.S. Geological Survey spectral library (Clark et al., 2007) and hydrous minerals are identified based on the spectral features. We also

Table 1
Relevant Spectral Parameters in the Study

Spectral parameter	Formulation
BD (1.9 μm)	1–2*MED (R191:R194)/(MED (R173:R185) + MED (R210:R216))
BD (Mg-OH)	1–2*MED (R229:R233)/(MED (R208:R218))
BD (2.35 μm)	1–2*MED (R234:R237)/(MED (R226:R231) + MED (R244:R248))
BD (Al-OH)	1–2*MED (R220:R225)/(MED (R213:R217) + MED (R225:R229))
BD (Olivine)	1.-AVG (R135,R140)/AVG (R170,R181)
BD (LCP)	1-AVG (R185,R215,R208)/AVG (R135 + R154 + R248 + R258)

Note. R### is the reflectance at a specific channel, for example, R190 stands for reflectance value at a wavelength of 1.9 μm. MED is the median, and AVG is the mean of the following channels in parentheses.

mapped the units with hydrous mineral detections based on CRISM spectral parameter maps in geographic information system software to better understand their distribution and correlation to morphology.

3.3. Other Data Sets

To further our understanding of the formation processes for the hydrous-mineral-bearing units in Lyot and its vicinity, we investigated data from the CTX (Malin et al., 2007) and High Resolution Imaging Science Experiment (HiRISE; McEwen, Eliason, et al., 2007) instruments onboard MRO and the THEMIS instrument onboard Mars Odyssey. We constructed a full coverage CTX mosaic over the Lyot crater using a nondestructive blending technique (Dickson et al., 2018) with CTX grayscale images acquired over visible and near-infrared wavelengths, at a resolution of ~6 m/pixel and in swaths of ~30 km. The HiRISE instrument, which has a resolution ~30 cm/pixel, also acquired imagery covering parts of the five impact craters. HiRISE acquires both grayscale and three-band color with the gray scale captured in ~6-km-wide swaths and the color acquired in ~1.2-km-wide swaths in the center of the grayscale image. We manually coregister higher-resolution CTX and HiRISE images with CRISM images where hydrous mineral detections are made to investigate the correlation of mineralogy with morphological units. Daytime and nighttime infrared image mosaics from THEMIS provided additional information on the thermophysical properties of relevant units (Edwards et al., 2011).

3.4. Crater Morphology and Excavation Depth Estimate

We extracted the geometric data for each of these five craters from the Mars Global Crater Database (Robbins & Hynek, 2012a; Table 2 and Figure 1) and calculated the maximum excavation depth for ejecta, approximated to 1/10 of the diameter of the transient crater (D_{exc} = 1/10 $D_{transient}$; Melosh, 1989). The diameter of the transient crater can be computed following the crater scaling relationship: $D_{transient}$ = a $(D_{final})^b$ $(D^*)^c$, where D^* is the transition crater diameter (~8 km for Mars; Garvin & Frawley, 1998); $D_{transient}$ is the diameter of the transient crater; D_{final} is the rim-to-rim diameter of the final crater; and a, b, and c are scaling depending on different scaling relationships (Croft, 1985; Holsapple, 1993; Melosh, 1989; see Table 3). We calculate the range of possible maximum excavation depths based on these scaling relationships for each crater. For deposits within crater central peaks, we also estimate the depth of origin of central peak materials based on an empirical relationship ($SU = 0.086*D^{1.03}$; Grieve & Pilkington, 1996).

To assess the degradation state of the craters, we compare the estimated morphology parameters for pristine craters to crater morphology. We report a calculated crater depth (d) between the values predicted by scaling relationships $d = 0.25D^{0.53}$ (Whitehead et al., 2010) and $d = 0.323D^{0.538}$ (Tornabene et al., 2018), where D is the diameter of the crater. These relationships are chosen to cover the range of values predicted based on the scaling relationships in previous Martian craters catalogs (Garvin et al., 2003; Robbins & Hynek, 2012b; Stewart & Valiant, 2006). Expected crater rim height (h) is calculated from scaling relationships: $h = 0.025D^{0.820}$ (Robbins & Hynek, 2012b) and $h = 0.02D^{0.84}$ (Garvin et al., 2003).

4. Results

4.1. Geological Investigation of Lyot Crater

With the analysis of CRISM, CTX, and HiRISE data, we have identified at least five distinguishable spectral classes and mapped out associations with rocks and sediments within and around Lyot crater.

Table 2
Summary of Hydrous Mineral Detections in Lyot Crater and Smaller Complex Craters in the Vicinity of Lyot

Crater ID	Crater name	Crater age	Latitude (degree)	Longitude (degree)	Diameter (km)	Rim to floor depth (km)	MOLA elevation (km)	Maximum excavation depth (km)	Hydrous mineral detections[a]			
									Central peak/ring	Crater wall/rim	Ejecta	Crater floor
05-000000	Lyot	Early Amazonian	50.46	29.31	220.3	3.14	−3.75	13–14	Fe/Mg sm, chl, hyd	chl, ill/mus, preh	Fe/Mg sm, chl, ill/mus, hyd	chl, ill/mus
05-000053	Micoud	Amazonian, probably younger than Lyot	50.56	16.35	50.3	1.55	−4.04	3.2–3.8	Fe/Mg sm, chl, preh, ill/mus, hyd	n.d.	no coverage	Fe/Mg sm, hyd
05-000308	Unnamed (c308)	Amazonian, younger than Lyot	49.09	20.99	22.4	1.29	−3.88	1.4–1.9	Fe/Mg sm, silica, hyd,	no coverage	n.d.	n.d.
05-000375	Unnamed (c375)	Amazonian, probably younger than Lyot	52.42	39.86	20.0	1.20	−3.59	1.3–1.7	chl	n.d.	n.d.	n.d.
05-000194	Unnamed (c194)	Hesperian-Amazonian	47.91	53.78	28.4	0.52	−3.05	1.8–2.3	-	n.d.	n.d.	chl

Note. Crater ID and geometry data are from Mars global crater database (Robbins & Hynek, 2012a).
[a]Mineral abbreviations: chl = chlorite; Fe/Mg = Fe/Mg smectite; ill/mus = illite/muscovite; n.d. = not detected; preh = prehnite; silica = hydrated silica; hyd = hydrated unidentified.

4.1.1. Spectral Properties and Distribution of Hydrous Minerals

The spectral class with weak 2.3-μm absorptions coexisting with 1.9-μm absorptions is found mainly on the peak ring of Lyot (Figure 2a). The detections have a weak Fe-OH or Mg-OH absorption (~0.5% lower reflectance than continuum) in channels between 2.29 and 2.31 μm and, typically, a coexisting weak 1.9-μm absorption related to H_2O. The position of these absorption bands is consistent with Fe/Mg phyllosilicate detections (Bishop et al., 2002; Clark, 1999), likely smectite or mixed-layer smectite-chlorite. The correlation of these spectral properties with features of discrete surface morphology suggests that these spectra are associated with geologic units of distinct compositions. The Fe/Mg phyllosilicates are mostly concentrated in the kilometer-sized knobs in the peak ring of Lyot (Figures 3 and 4).

The spectral class with a strong (and broad) 2.35-μm absorption band is identified as chlorite (Figure 2b), consistent with the library spectra of chlorite with a strong Mg-OH absorption at 2.35-μm and a weak 1.9-μm H_2O absorption (Bishop et al., 2008). In Lyot crater, chlorite detections often appear in spatial mixtures with other phases, including Fe/Mg phyllosilicate, illite/muscovite, or prehnite, which causes variations in band position and width. Chlorite detections are widely distributed in Lyot crater (Figure 3), mostly found associated with bedrock units in the peak ring and terraced rim of the crater. Chlorite is also the most common spectral class associated with Lyot's proximal ejecta.

A distinct class of spectra is found with a 2.21-μm absorption coexisting with a 2.35-μm absorption (Figure 2), sometimes associated with 1.4- and 1.9-μm bands. This is identified as illite or muscovite, matching the spectral features of mica or high-charge phyllosilicates (e.g., vermiculite and mixed illite-smectite) with both sharp 2.21- and 2.35-μm absorptions (Clark et al., 1990). The width of the 2.21-μm feature is inconsistent with that of hydrated silica, which has a broader absorption (Anderson & Wickersheim, 1964; Milliken et al., 2008). In Lyot, illite/muscovite always occurs in close proximity to chlorite/prehnite features (Figure 3). Spatial mixing with nearby chlorite is a possible explanation of the strong 2.35-μm feature, often equivalent to or stronger than the 2.21-μm feature. Illite/muscovite has been identified previously in the southern highlands (Carter et al., 2013; Ehlmann et al., 2009; Fraeman et al., 2009) and often co-occurs with chlorite minerals (e.g., Ehlmann et al., 2009),

Table 3
Scaling Parameters for Complex Crater's Transient Crater Diameter Used

Parameters	a	b	c
Melosh, 1989	0.65	1	0
Holsapple, 1993	0.758	0.921	0.079
Croft, 1985	1	0.85	0.15

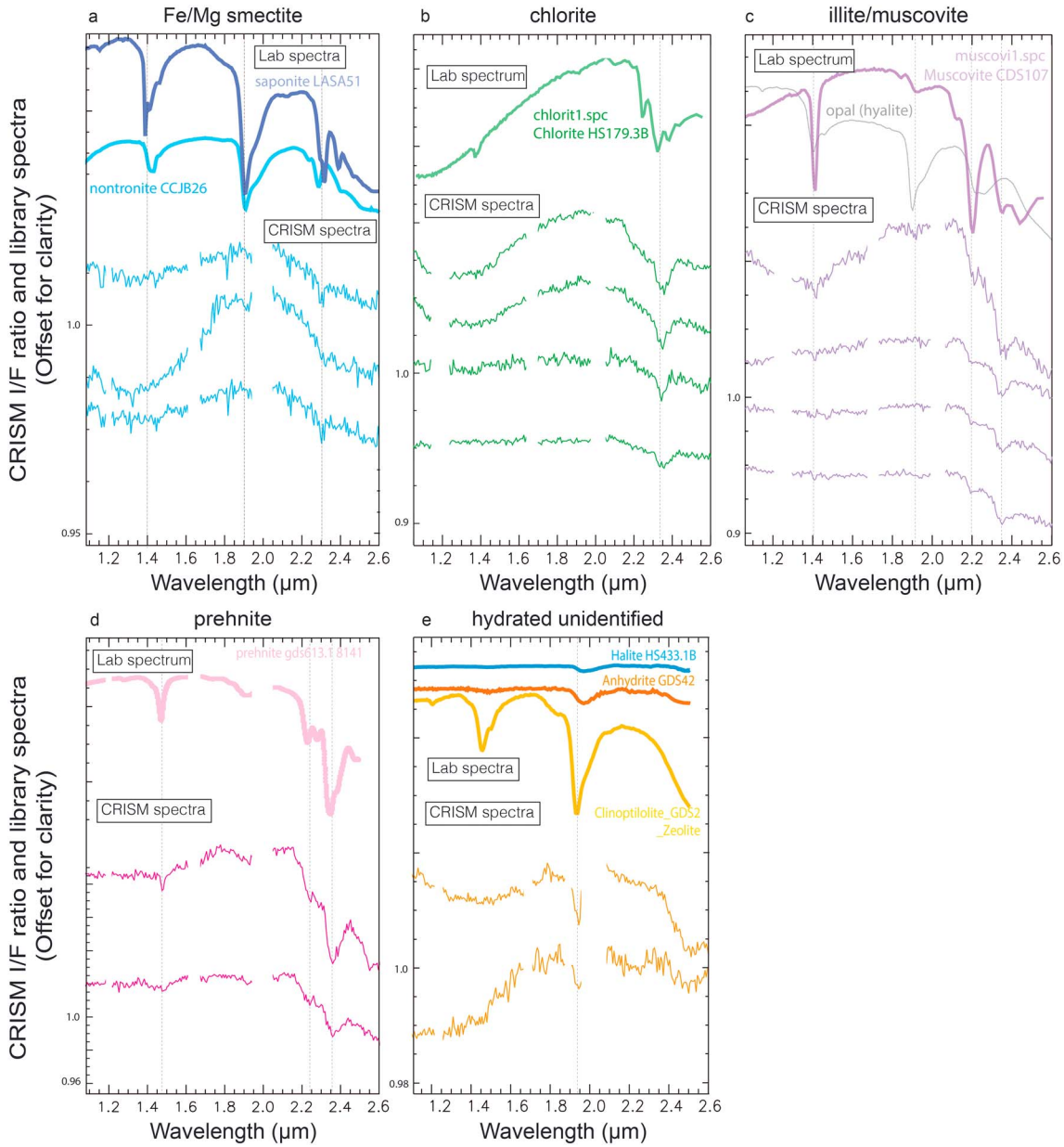

Figure 2. CRISM spectra and associated library spectra of hydrous minerals identified in Lyot crater. (a) Fe/Mg phyllosilicate detections, likely smectite or mixed-layer smectite-chlorite. (b) Chlorite is detected with a strong 2.35-μm absorption band, in most cases lacking 1.9 μm. (c) Illite/muscovite is identified with a 2.21 μm coexisting with a 2.35-μm absorption. A spectrum of hydrated silica (opal) is shown for comparison of the 2.21-μm band. (d) Prehnite is identified by distinctive 1.47- to 1.48-μm absorption coexisting with 2.2- and 2.35-μm bands. (e) Unidentified hydrated minerals with only 1.9-μm absorptions and possible 2.5-μm bands. Here we show the library spectra of (hydrated) halite, anhydrite, and zeolite spectra with possible matching features. The lab spectra of saponite and nontronite are from CRISM spectral library, and all other lab spectra are from USGS spectral library (Clark et al., 2007). The CRISM image ID and coordinates of the central pixel the spectra are extracted from are given in Table A1. CRISM = Compact Reconnaissance Imaging Spectrometer for Mars; USGS = U.S. Geological Survey.

but within the northern lowlands, it is only found to occur in the Lyot vicinity (Carter et al., 2013; Pan et al., 2017).

The spectra with distinctive 1.47- to 1.48-μm absorption coexisting with 2.23- to 2.24-μm and 2.35-μm absorptions (Figure 2) is a different class associated with the mineral prehnite. The existence of a 1.48-μm absorption and its weak 2.2-μm feature at longer wavelengths distinguish the prehnite from illite/muscovite. Prehnite is a Ca- and Al-rich inosilicate mineral that forms in hydrothermal or metamorphic environments on Earth. The occurrence of prehnite indicates an elevated temperature of at least ~200 °C and is a typical product in low-grade metamorphism (Robinson, 1987). Prehnite is not found within the crater or

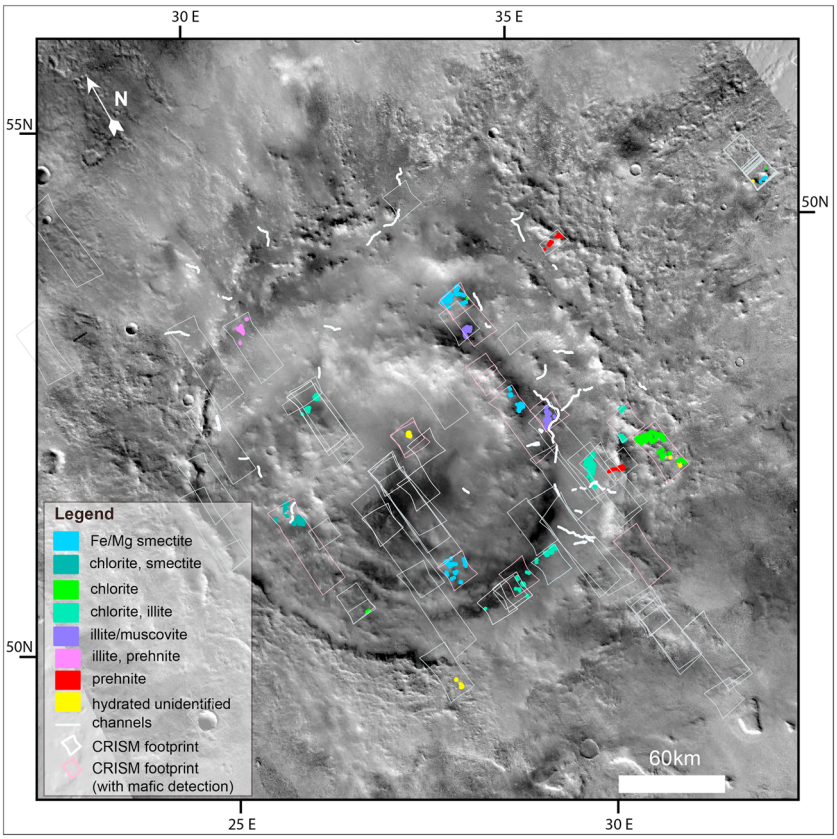

Figure 3. Distribution of the detections of different spectral classes from CRISM data on a CTX mosaic of Lyot crater, with fluvial channels mapped inside the crater. Outlines of CRISM data show the coverage and images examined for mineral detections. CRISM = Compact Reconnaissance Imaging Spectrometer for Mars; CTX = Context Camera.

on the ejecta blanket, but only in three occurrences on the crater rim of Lyot (Figure 3). Prehnite detections in Lyot sometimes occur in close proximity to illite/muscovite and chlorite deposits.

The last spectral class with a distinctive 1.9-μm absorption lacks other diagnostic well-defined absorption bands in the 2.1- to 2.5-μm region (Figure 2e). This type of spectra could be explained by a zeolite with absorptions only at 1.9 and 2.5 μm, a hydrated chloride or polyhydrated sulfates with drop-off at 2.4 μm. Alternatively, these could be other kinds of hydrated silicate minerals with enhanced water absorptions relative to metal-OH absorptions due to change in relative humidity, while the absorptions in the 2.1- to 2.5-μm region are weak and cannot be distinguished from noise in the CRISM spectra. In Lyot crater the unidentified hydrated mineral occurs in the central peak as well as on the ejecta blanket (Figure 3).

4.1.2. Morphology of Hydrous Mineral Units

As the previous mapping in Lyot based on CTX data showed, several different surface morphologic units are present in Lyot crater (Dickson et al., 2009). Based on observations of the superposition relationships between the different units, the identified units from older to younger ages are (1) a bedrock unit with knobs and mesas in the peak ring, the terraced crater rim, and the crater floor; (2) a stippled mantling unit that embays the knobs and mesas; (3) the sinuous channels and fans in the fluvial valley system; and (4) a smooth mantling unit that often occurs on sloping surfaces interpreted to be mass-wasting products from the uplifted bedrock. Previous work on the chronology indicates emplacement of the stippled mantling unit in the mid-late Amazonian after the Lyot impact, and then the channels and fans formed, cross-cutting or overlying the mantling unit in the late Amazonian (Dickson et al., 2009).

In the peak ring, Fe/Mg smectite and chlorite detections are found spatially associated with topographic highs of the bedrock unit (Figures 4 and 5), though fresh bedrock is not apparent due to mantling. Near the crater rim, chlorite detections co-occur with illite/muscovite in eroded bedrock units (Figure 6), but they sometimes also occur in the smooth mantling units near these topographic highs (Figures 7b and 7c). The

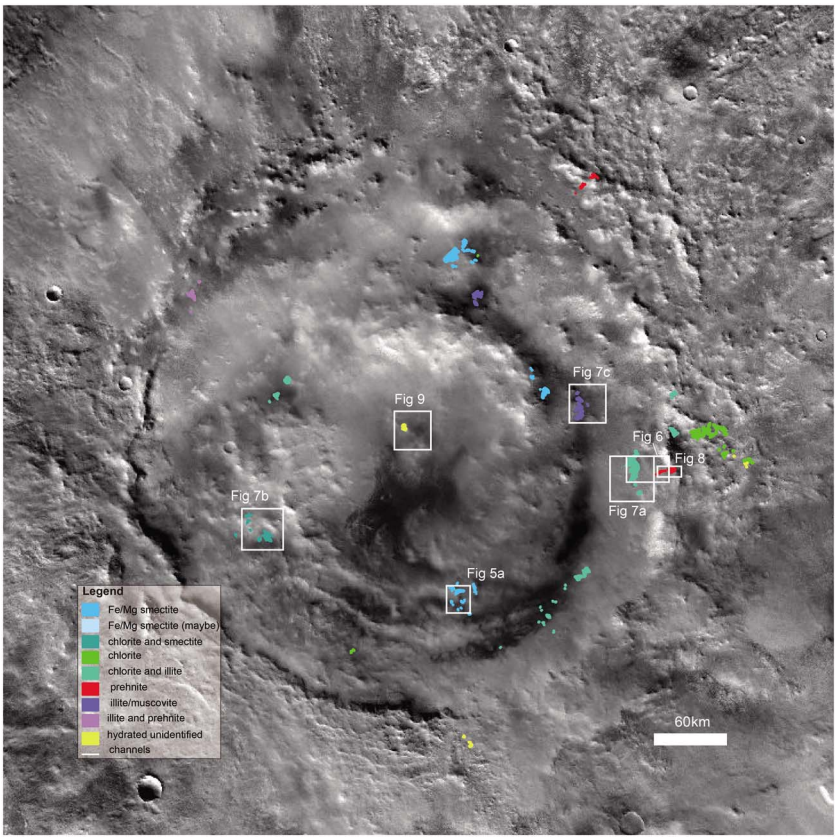

Figure 4. Lyot crater mineral map as in Figure 3 the locations of Figures 5–9 indicated. See Table A2 for a full list of the relevant image IDs and projections for the following figures.

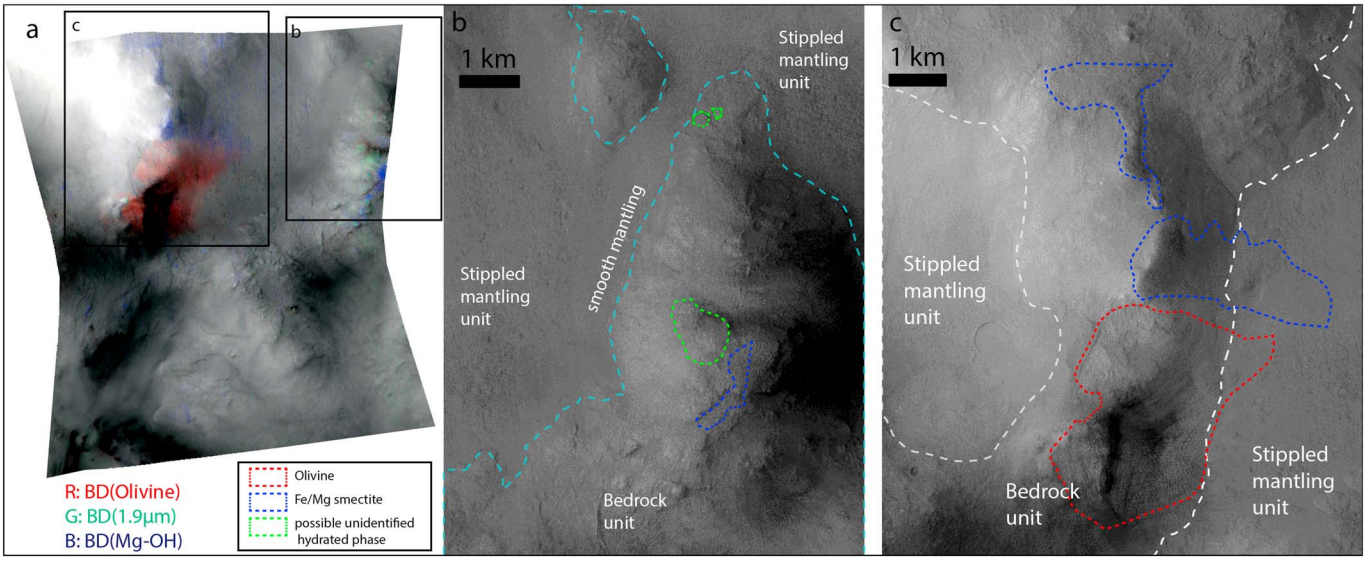

Figure 5. Fe/Mg smectite bearing units in Lyot crater peak ring. (a) CRISM image (FRT0000CB40) spectral parameter overlay, where red is olivine; green is unidentified hydrated mineral; blue is Fe/Mg smectite. (b and c) Digitized mineral detections on CTX image D02_027864_2294_XN_49N330W. CRISM = Compact Reconnaissance Imaging Spectrometer for Mars; CTX = Context Camera.

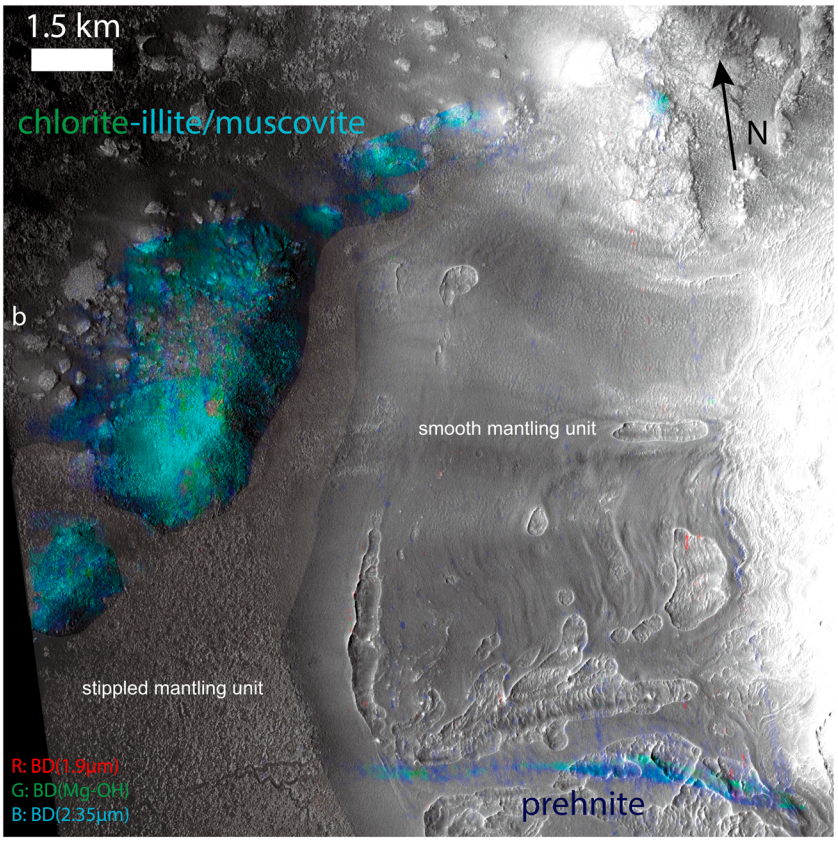

Figure 6. Chlorite and illite/muscovite detections in the lower levels of the terraced crater wall of Lyot. The detections correlate with degraded knobs embayed by stippled mantling unit. The prehnite detection is located near the crater rim on the smooth mantling units, comprised of materials that have been transported downslope. Spectral parameter map of CRISM image (FRT00020B25) is shown with the color composite of R: BD (1.9 μm) G: BD (Mg-OH) B: BD (2.35 μm). Background is CTX image D19_034602_2296_XN_49N328W in simple cylindrical projection). CRISM = Compact Reconnaissance Imaging Spectrometer for Mars; CTX = Context Camera.

orientation of the materials down the topographic gradient from the bedrock highs suggests that the detections are of mass-wasting products derived from the bedrock unit. Prehnite has the most distinctive distribution only found close to the crater rim (Figure 3) with two locations on the eastern part of the crater and one on the northwest crater rim location in mixture with illite/muscovite. One prehnite outcrop can be traced from the crater rim to within the crater, following topographic lows, with a morphology consistent with mass wasting of 3- to 4-km distance (Figures 6 and 8). The trace of prehnite-bearing sediments cannot be correlated with the surface morphology in the overlapping HiRISE image (Figure 8), but it is located immediately downslope of the prehnite detection on the rim and small channels incising the mantling unit follow the downslope direction of the mass-wasting deposit. The unidentified hydrated mineral found in the central peak image is correlated with a bedrock exposure with light-toned, fractured unit in the central peak (Figure 9).

Sinuous, kilometer-long channels have been mapped in Lyot cutting across the stippled mantling unit (Dickson et al., 2009). These channels form in topographic lows in between the high-standing bedrock (Figures 7a–7c), diverting around the bedrock knobs (Figure 3), incising the mantling unit. This relationship demonstrates that the fluvial activity forming sinuous channels started later than the emplacement of mantling units, which embay the phyllosilicate/chlorite-bearing bedrock units. Thus, the sinuous channels did not contribute to the formation of these hydrous minerals but rather played a role in exposing them. Based on cross-cutting relationships, the channel-formation marks the latest aqueous event within Lyot crater.

4.1.3. Scouring Channels to the North of Lyot

Channelized scablands are found to the north of Lyot outside the ejecta blanket (Harrison et al., 2010) with only a few small, morphologically distinct channels recently identified on the ejecta (Weiss et al., 2017).

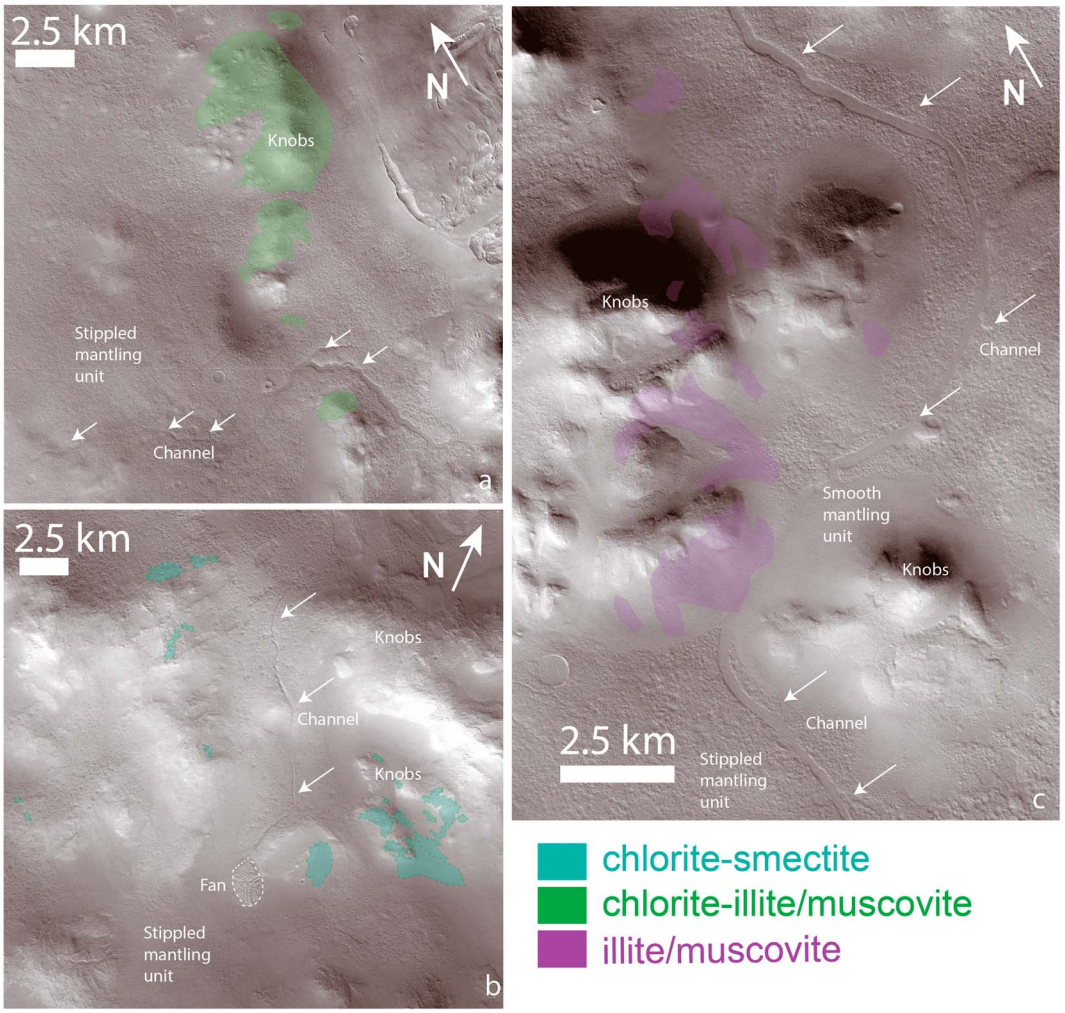

Figure 7. Representative sinuous channels that transect knobby regions in Lyot crater with hydrous mineral detections. White arrows indicate the sinuous channels in each image. Channels are diverted around landforms with hydrous mineral detections: (a) chlorite and illite/muscovite, (b) chlorite and Fe/Mg phyllosilicate, and (c) illite/muscovite. The background image is a CTX mosaic in Mars North Polar Stereographic Projection, and the outline of hydrous mineral detections are mapped out based on CRISM detections (FRT00029B25, FRT00023F1F, and FRT00021FCB). CRISM = Compact Reconnaissance Imaging Spectrometer for Mars; CTX = Context Camera.

Thirty-two CRISM-targeted images were examined (see Table A3) north of Lyot crater covering the region where fluvial channels have been previously identified, and we did not identify any hydrous minerals.

4.2. Mineralogy of Complex Craters in Lyot's Vicinity

4.2.1. Micoud Crater

Micoud crater (D = 50 km) is a complex crater with a terraced rim situated to the west of Lyot. Micoud has been partially filled by a mantling unit that has been later eroded, evidenced by a buried small crater near the central peak. Micoud crater's impact ejecta were emplaced atop the late Hesperian plains material, same as Lyot crater (Figure 1). The interior of Micoud is covered by a mantling unit that has been eroded. The stratigraphic relationship with other northern plains units, fill, and overall degradation state is similar to Lyot crater. The secondary crater field of Lyot (Robbins & Hynek, 2011) extends to the west of Micoud but becomes less prominent within and near Micoud crater, which suggests a similar but possibly younger formation age than Lyot, in the Amazonian.

Micoud crater has the same set of diverse hydrous minerals as Lyot, including Fe/Mg smectite (with possible carbonate detection, in this case), chlorite, illite/muscovite, prehnite, and an unidentified hydrated mineral

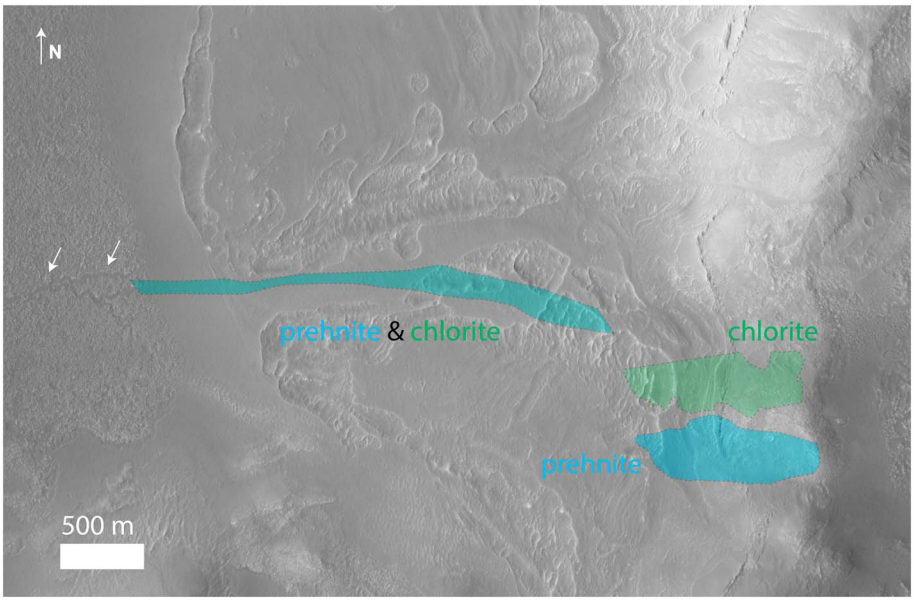

Figure 8. Detailed morphology of the prehnite and chlorite bearing units on the crater rim and the linear feature with prehnite and chlorite spectral signature near the crater rim seen in Figure 6. The regions of hydrous minerals are highlighted and outlined based on CRISM images (FRS0002CB59 and FRT00020B25) coregistered to CTX image (D19_034602_2296_XN_49N328W). The elongated shape of the prehnite and chlorite detections on the slope next to the crater rim indicates mass wasting of the mineral-bearing materials. White arrows show the small channels in the stippled mantling unit, just downslope of the mass-wasting deposit. CRISM = Compact Reconnaissance Imaging Spectrometer for Mars; CTX = Context Camera.

(Figure 10). Except for one crater floor deposit, most hydrous minerals are concentrated in the degraded central peak of Micoud, in discrete units (Figure 11a).

Two different spectral classes with 2.3-μm absorptions are found in Micoud (Figure 10a). One is found close to the central peak, with a sharper and narrower 2.3 μm and a possible 2.5 μm band, in addition to 1.4- and 1.9-μm bands due to H_2O and OH. The presence of 2.5-μm absorption agrees with magnesium carbonate spectra, which have C–O overtones at ~2.31 and ~2.51 μm (Gaffey, 1987), but the width of the 2.3-μm band is narrow, which matches better with nontronite than magnesite, though the 2.4-μm band often present in nontronite is not observed. There is no clear correlation of the band depths of the 2.3- and 2.5-μm bands, since the detections are limited to small regions. A second spectral class has much broader, asymmetric 2.3- and 2.5-μm absorptions, which may be explained as carbonate or Fe/Mg smectite mixing with phases with a longer 2.35-μm feature such as chlorite or Fe-serpentines. This type of spectra is found mantling the complex zone of bedrock displaced as lower wall terraces and fallback breccia. Regardless of the phase(s) responsible, the 2.3-μm absorptions in these Micoud spectra are stronger and broader than what we see in Lyot. The hydrous mineral present in Micoud with 2.3- and 2.5-μm absorptions is mapped as Fe/Mg smectite, though coexistence of intermixed carbonate is possible.

Chlorite is also detected in Micoud's central peak (Figures 11 and 12). The 2.35-μm absorption is broad and associated with a weak 1.9-μm absorption. Sometimes, the chlorite spectra exhibit a 2.5-μm absorption, similar to the second type of Fe/Mg smectite described above (Figure 10b). These chlorite detections are likely in mixture with Fe/Mg smectites. Illite/muscovite and prehnite detections occur in the same general region within the central peak (Figure 12). Several pixels close to the illite/muscovite have a 1.48-μm absorption band that matches prehnite (Figures 10c and 12). These spectra are similar to the spectra of illite/muscovite and prehnite in Lyot and are found adjacent to mafic-mineral-bearing light-toned bedrock (Figures 12c and 12d). Occurring on the side slope of bedrock, it is unclear if chlorite detections are associated with a mantling material or with the bedrock that is different in composition. An unidentified type of hydrated mineral is also found in a small portion of the light-toned fractured material in Micoud central peak (Figure 10b), near more widespread chlorite detections and localized prehnite and illite/muscovite detections adjacent to the region of mafic-mineral-bearing rocky units.

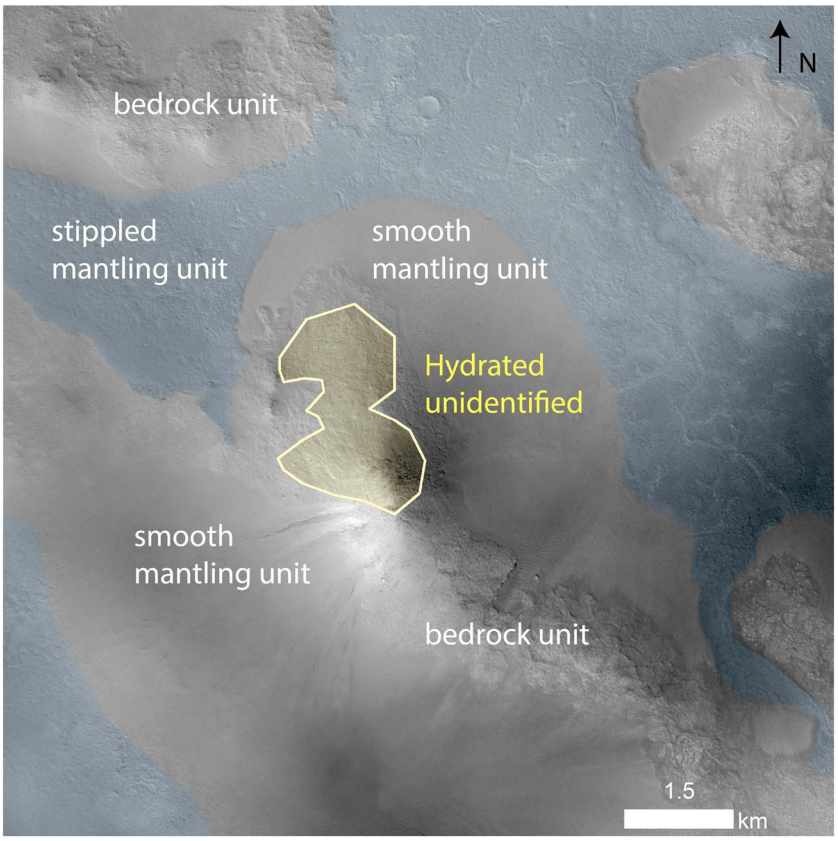

Figure 9. Lyot crater central peak region with a detection of an unidentified hydrated mineral on the bedrock unit. Mineral mapping is based on CRISM image (FRT0000B133). The background image is HiRISE image ESP_027376_2310 in simple cylindrical projection. CRISM = Compact Reconnaissance Imaging Spectrometer for Mars; HiRISE = High Resolution Imaging Science Experiment.

4.2.2. Crater c308

c308 is a complex crater (diameter, 22 km) ~240 km west of Lyot crater rim. Its crater ejecta overlies the eroded margin of the distal ejecta blanket of Lyot, and the ejecta blanket is well preserved with no sign of disruption by Lyot crater. Thus, c308 likely formed after Lyot. Two kinds of spectra with a strong 2.3-μm band coexisting with 1.9- and 1.4-μm bands have been identified and classified as Fe/Mg smectite (Figure 10a). Similar to Micoud, these spectra with 2.3-μm bands are accompanied by possible 2.5-μm absorptions, with varying relative depths and widths. The varying band width and depth may be induced by varying degrees of mixing with a carbonate endmember that has wider 2.3-μm band than Fe/Mg smectite. In c308, we also detect the presence of hydrated silica, with a broad band at 2.2 μm as well as an additional 1.9-μm band (Figure 10c). An unidentified hydrated mineral is also present (Figure 10b). These hydrous mineralogies are concentrated in the central peak region (Figure 13), sometimes associated with exposed bedrock and mass-wasting products near those exposures, with distinct surface texture from that of the light-toned mafic-mineral-bearing block (Figures 13f and 13g).

4.2.3. Crater c375

c375 is a 20-km-diameter crater on the distal ejecta blanket of Lyot, which also postdates the Lyot impact. It has been previously studied as unnamed Ismenius Lacus impact crater (Turner et al., 2016). The crater is partially filled with later mantling units and has a central mound ~4.2 km in diameter, ~500 m in height in the center of the crater (Figure 13). This mound is smooth and the blocky central peak materials are mantled by sedimentary debris, with channels incising mantling materials. Unlike Lyot, Micoud, and c308, chlorite is the only hydrous mineral detected here in the central mound (Figure 10b), confirming the detection made by Turner et al. (2016). Active gully formation creates new fan deposits in the central mound, and the chlorite detections are found on dust-free surfaces in the central mound as well as in the fine-grained sediments at the base of the mound (Figures 11c and 14). In addition, there is a prominent linear, light-toned feature

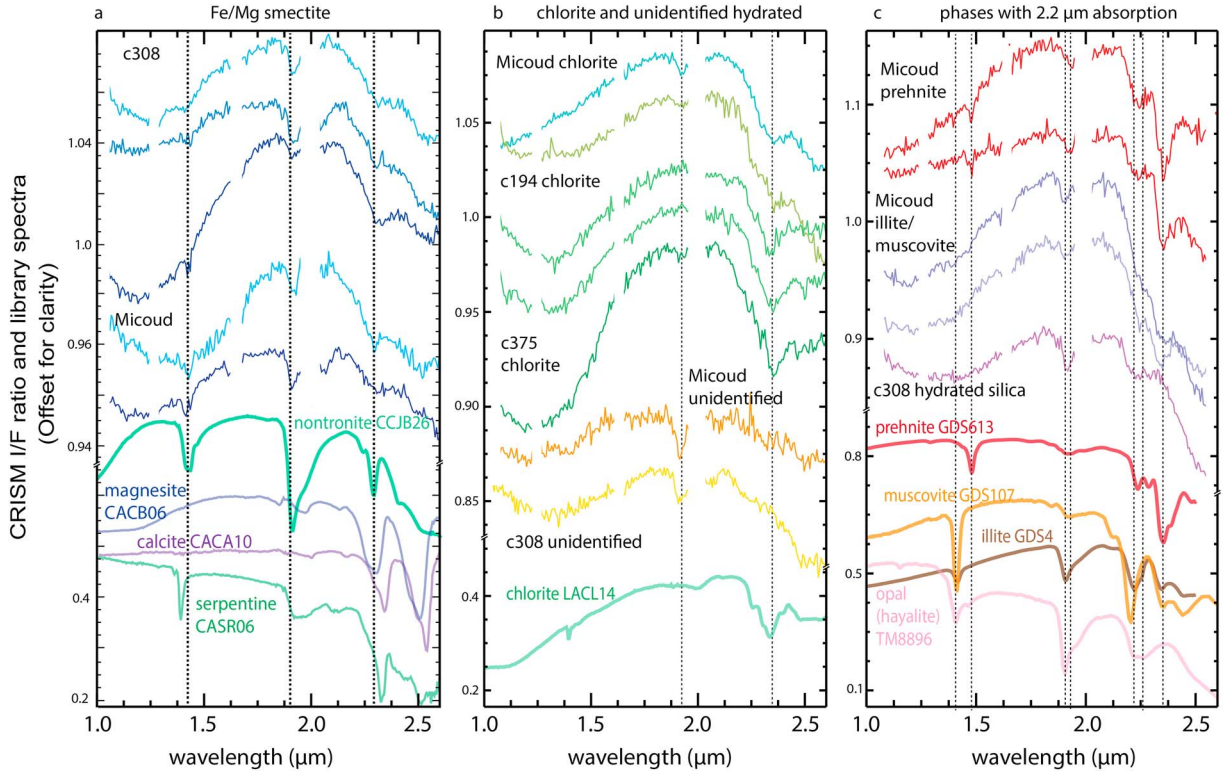

Figure 10. CRISM ratioed I/F spectra of hydrous minerals identified in smaller complex craters around Lyot compared to lab spectra (Clark et al., 2007). (a) Fe/Mg phyllosilicate detections in Micoud and c308. (b) Chlorite detections in Micoud, c194 and c375 with a strong 2.35-μm absorption and unidentified hydrated detection in Micoud and c308. The chlorite detections in c194 and c375 lack 1.9-μm band as typical chlorite, but the detection in Micoud has the additional 1.9-μm feature. (c) Less frequently appearing phases with 2.2-μm absorptions are shown in this panel. Prehnite detection is found with a 1.48-μm band in two outcrops in the central peak of Micoud crater; illite/muscovite is identified with a 2.21 μm coexisting with a 2.35-μm absorption, with a weak 1.41-μm band. In c308, we detect the presence of hydrated silica with a broad band at 2.2 μm as well as additional 1.4-μm band, distinct in spectral properties from the other detections. Wavelength regions with known CRISM artifacts and residual of atmospheric correction are masked. Lab spectra are from USGS spectral library (Clark et al., 2007). The CRISM image ID and coordinates of the central pixel the spectra are extracted from are given in Table A1. CRISM = Compact Reconnaissance Imaging Spectrometer for Mars; USGS = U.S. Geological Survey.

~1 km in length and up to 200 m in width within the eastern slope, which is spatially correlated with the chlorite detection (Figures 14b and 14d). The linear, light-toned feature has a sharp, abrupt boundary at the interface with the surrounding materials.

4.2.4. Crater c194

c194, with a crater diameter of 28 km, is within the Hesperian-Noachian unit. The crater rim elevation varies from −2,750 m (relative to MOLA datum) on the northwest side to −2,350 m on the southeast side, but the crater fill is relatively homogeneous in elevation with the minimum at around −3,100 m. The crater depth varies between ~350 and ~750 m, which is much shallower than the expected crater depth (~1.46 to ~1.94 km) predicted for pristine Martian craters (see section 3). Both the shallow depth and the absence of a central peak indicate that the crater is heavily degraded by erosion and infill. These infilled sediments form a concentric ridged surface inside the crater (Figure 11d), consistent with typical concentric crater fill widespread in the region (Levy et al., 2010). This infill unit has been proposed to form via successive episodes of sublimation of near-surface ice.

Only dark patches of the infill unit have the concave continuum and strong 2.35-μm band typical of chlorite (Figures 10b and 11d). The dark region is located in the northeast part of the crater in a local topographic low at the transition between the steep crater wall with ~300-m relief and the flat crater floor with infilled sediments (Figure 15). Though dark in the visible-near-infrared (HiRISE and CTX), the area is brighter in the THEMIS nighttime infrared image compared to surrounding units, indicating a higher nighttime temperature and thus higher thermal inertia compared to the surrounding surface. The presence of the decameter-scale ridges or terraces (Figure 15) and the higher thermal inertia of the chlorite-bearing deposits are consistent with higher degree of induration of the underlying crater fill compared to the surrounding units.

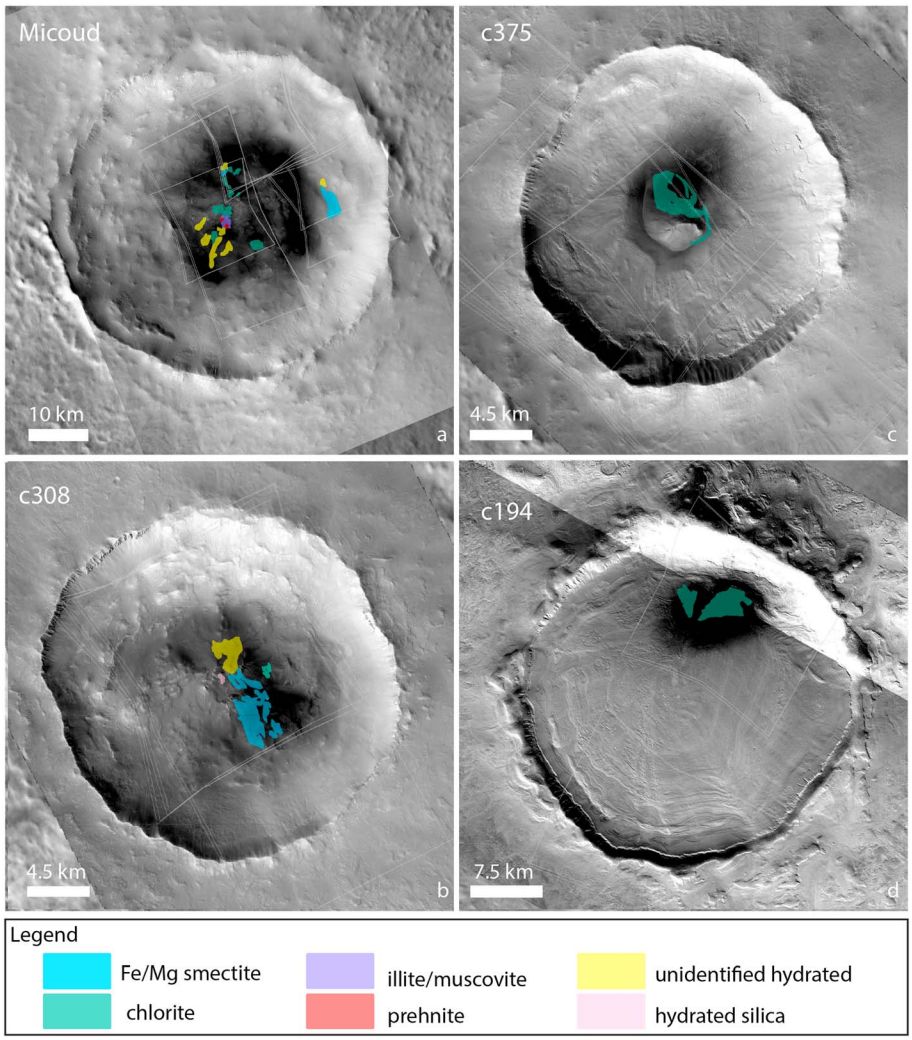

Figure 11. Distribution of hydrous minerals in craters in the vicinity of Lyot: (a) Micoud, (b) c308, (c) c375, and (d) c194. Multiple hydrous minerals have been found in Micoud and c308, distributed in the central peak region, but only chlorite has been identified in c375 and c194, associated with distinct morphologic features, respectively.

4.3. Subsurface Ice Deposit and Hydrous Minerals in Deuteronilus Mensae

We surveyed thoroughly the CRISM images in the regions with subsurface ice deposits to better understand their relationship to hydrous mineral formation (Figure 16 and Table A4). We found an illite/muscovite detection ~250 km to the south of Lyot crater rim, around the same elevation as the Lyot preimpact surface (−3,510 m relative to MOLA). Fe/Mg phyllosilicate is found in small knobs and on the wall of channels and mesas further south (300–400 km from the Lyot crater center) located at a higher elevation (−2,000 to −3,000 m relative to MOLA), as well as in a steep-walled impact crater at the southwesternmost extent of the study area occurring with hydrated silica detections on the crater floor. The above hydrous detections occur on small knobs or slopes of mesas (e.g., Figure 17), while the lobate debris aprons with subsurface ice detections in the study region have dusty surfaces and do not show different spectral properties from the surrounding units.

5. Discussion

5.1. Relationship of Hydrous Mineralogy to Fluvial Geomorphology

In search for associated mineralogical traces of fluvial activities, we find no hydrous mineral detections associated to the fluvial channels north of Lyot extending from its ejecta blanket, which are a sign of postimpact, and likely impact-induced, fluvial activity (Harrison et al., 2010; Weiss et al., 2017), in contrast to the diverse

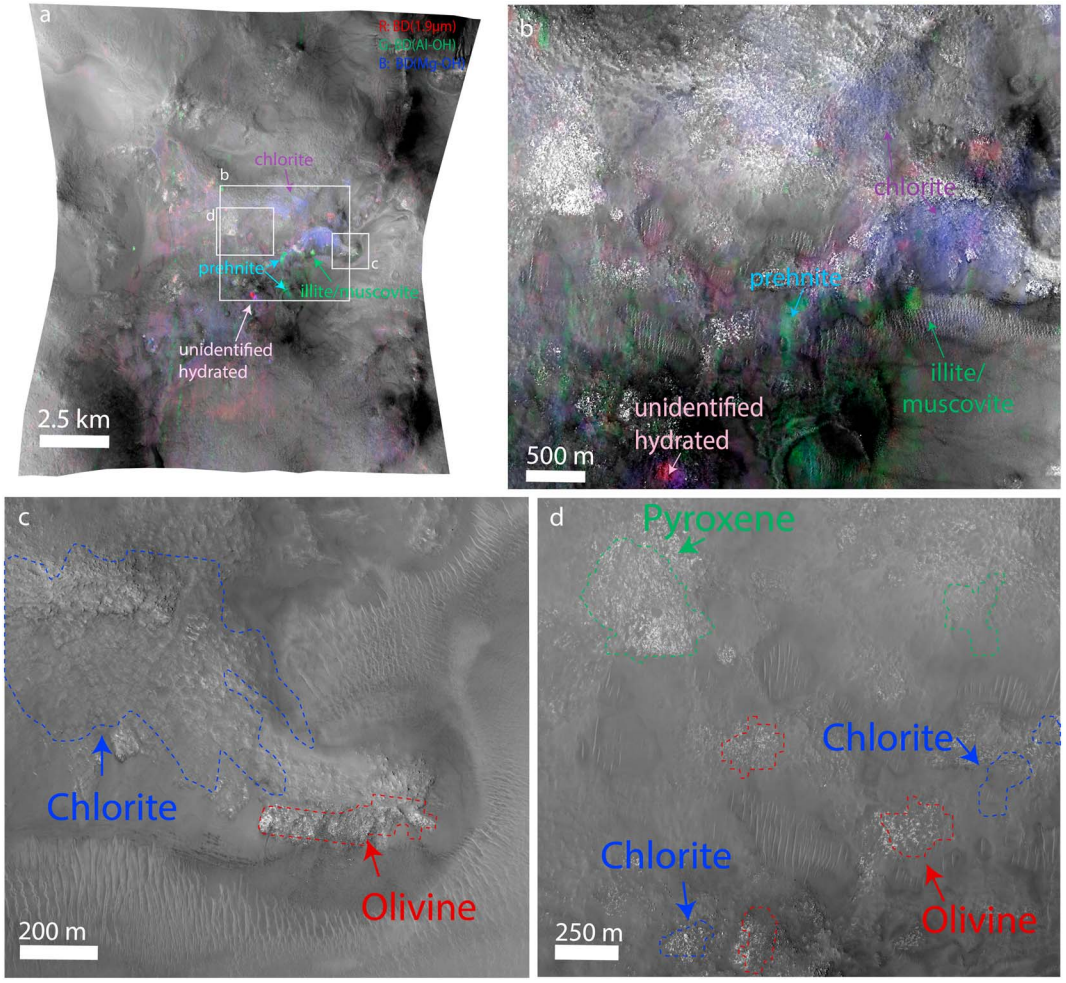

Figure 12. CRISM detections of hydrous minerals in the central peak region of Micoud crater. (a) Colored CRISM spectral parameter map (from image FRT00019658) overlay. The different colors represent different hydrous mineralogy as indicated on the figure (purple: chlorite; green: illite/muscovite; greenish blue: Prehnite; red: hydrated unidentified). (b) Zoom-in of CRISM parameters for hydrous mineralogy overlain on HiRISE (PSP_009997_2310) data. (c and d) Mineral detections digitized based on spectral parameter maps from CRISM image (HRL0000C75D) overlain on HiRISE (PSP_009997_2310), showing the spatial relationship of mafic and hydrous mineral detections. CRISM = Compact Reconnaissance Imaging Spectrometer for Mars; HiRISE = High Resolution Imaging Science Experiment.

hydrous mineralogy found within Lyot crater and other smaller craters. Although dust cover may mask some potential mineral detections, we find it unlikely that dust cover is the sole reason for the lack of detection of hydrous minerals, in particular with various exposures of smaller complex craters and scarps in this region and the relatively light dust cover compared to Deuteronilus Mensae (Ruff & Christensen, 2001), where hydrous minerals have been identified. Thus, we interpret that the channel formation events did not generate pervasive alteration and that the formation of the hydrous minerals inside craters is likely a distinct event from the channel formation to the north of Lyot. The lack of mineralization associated with these channels implies a rapid and probably low-temperature formation process, consistent with the melting of surface ice/snow from hot ejecta or dewatering of an ejecta blanket (Harrison et al., 2010; Weiss et al., 2017), instead of impact-induced groundwater circulation. Indeed, Weiss et al. (2017) estimate that only 10^2 to 10^3 years of erosion from melt of surface or near-surface ice beneath the ejecta are required to carve the channels. For acid weathering in Mars relevant conditions, kinetic and thermodynamic models predict some secondary minerals (e.g., amorphous silica) start to form for a duration of 10^2 to 10^3 years, but the volume is below 1% (Zolotov & Mironenko, 2007), which would be too low to detect from orbit. Given the uncertainties of initial pH, pressure, grain size, water to rock ratio, and degree of exposure, the duration required for secondary alteration may vary up to several orders of magnitude (e.g., Velde &

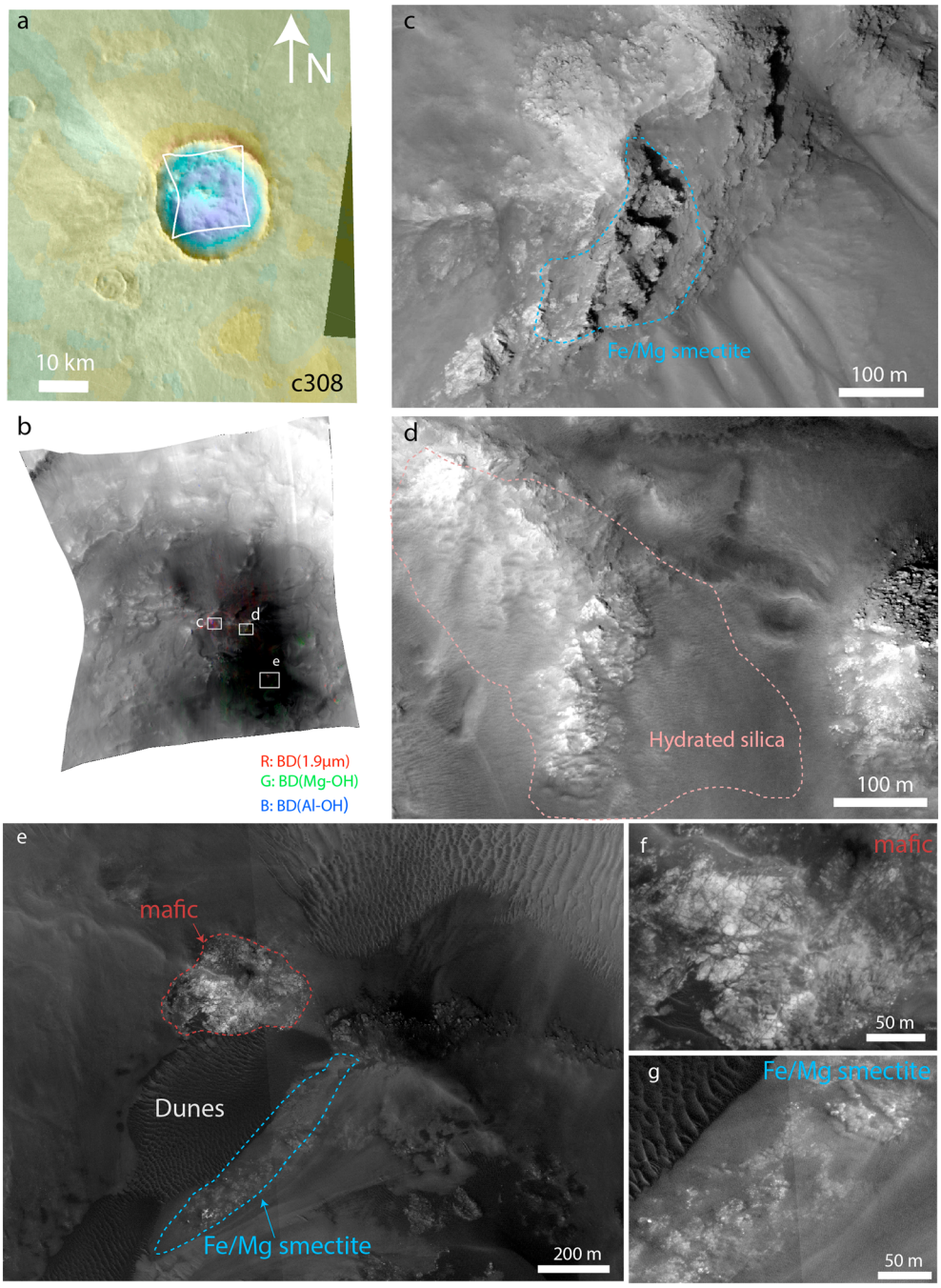

Figure 13. Geologic context of hydrous minerals in crater c308. (a) MOLA elevation overlain on THEMIS daytime infrared data on crater c308 in Mars North Polar Stereographic Projection, showing the context for CRISM image FRT00017D51. (b) CRISM color overlay with spectral parameter maps, with spectral signature associated the dark regions in the central peak. (c–e) Zoom-in on particular locations with CRISM detection on HiRISE image ESP_025082_2295. (f and g) Zoom-in showing the different textures of mafic-bearing and smectite-bearing units in (e). CRISM = Compact Reconnaissance Imaging Spectrometer for Mars; HiRISE = High Resolution Imaging Science Experiment; MOLA = Mars Orbiter Laser Altimeter; THEMIS = Thermal Emission Imaging System.

Meunier, 2008; Zolotov & Mironenko, 2007), but it is possible that the time span of liquid water that formed these channels may be too short for extensive mineralization that is sufficient to be detectable from orbit.

Within Lyot, no hydrous minerals are found in association with the stippled mantling unit, but some of the smooth mantling units in Lyot have chlorite or illite/muscovite features, which usually occur next to

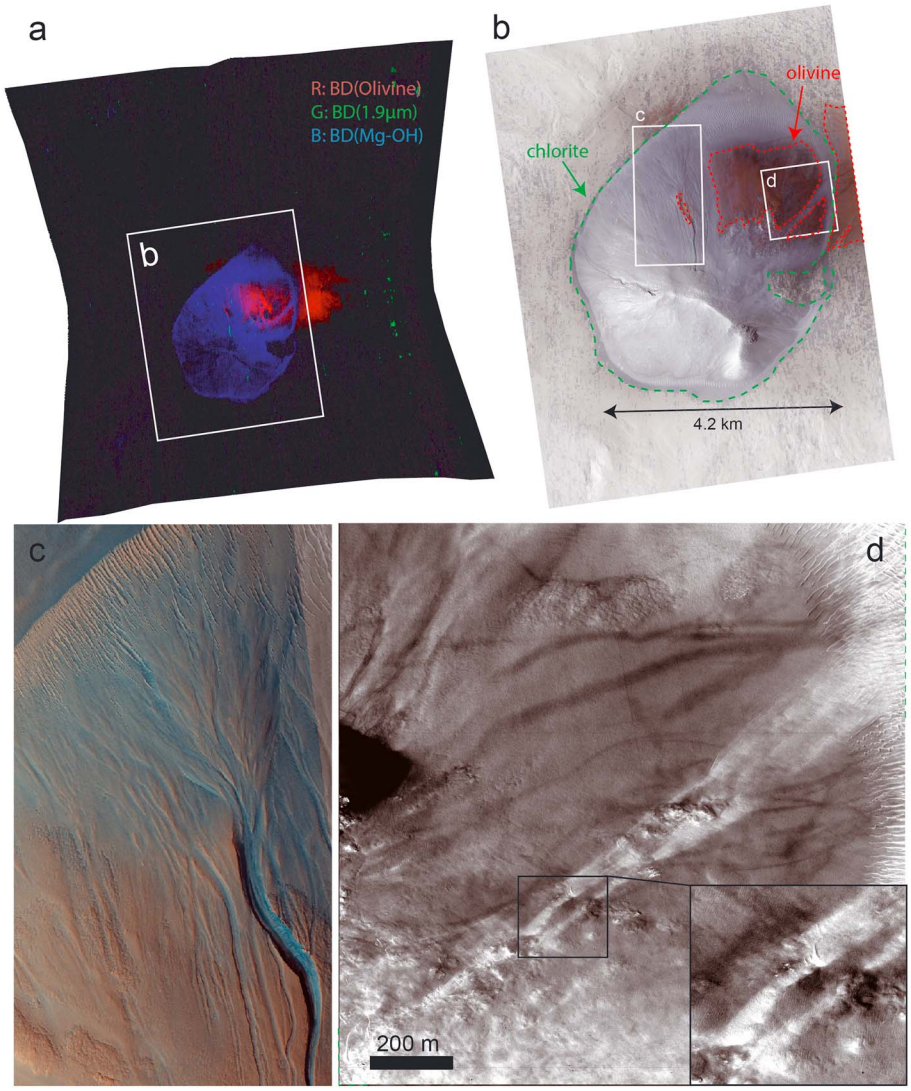

Figure 14. The central mound of crater c375 where chlorite was detected. (a) Spectral parameter map from CRISM image (FRT0000BFA6) covering crater c375. (b) HiRISE image (ESP_044149_2325) of the central mound overlain by color composite in a), showing the context for insert c and d. (c) Active gully and fan forming on the northern flank of the mound. From HiRISE color image, the fan has a bluish hue compared to the other parts of the mound, indicating fresh, dust-free surface. (d) A linear, light-toned feature in the mound ~1 km in length. Insert showing the light-toned feature across the bedrock exposures on the central mound. CRISM = Compact Reconnaissance Imaging Spectrometer for Mars; HiRISE = High Resolution Imaging Science Experiment.

bedrock units with the same mineralogy. This implies that the hydrous minerals in the mantling units may be sourced locally from the adjacent bedrock units. In addition, sinuous channels on the crater wall are observed to be incising and thus postdating the mantling units and are diverted by the hydrous-mineral-bearing knobs and mesas (Figure 7). Therefore, sinuous channels and fans represent a separate stage of aqueous activity in Lyot crater, which postdates the mantling units and the hydrous mineral forming units. Again, this episode of water activity appears unrelated to the formation of the hydrous mineral units detected from orbit within Lyot.

5.2. Formation of Hydrous Minerals in Lyot

Since the fluvial features are not responsible for the hydrous mineral formation, we consider two different mechanisms for the formation of these hydrous minerals within Lyot: (a) a syn-impact alteration scenario where hydrous mineral within Lyot crater formed during an impact induced hydrothermal system and (b) a preimpact formation scenario where hydrous minerals form in the subsurface and are then excavated by

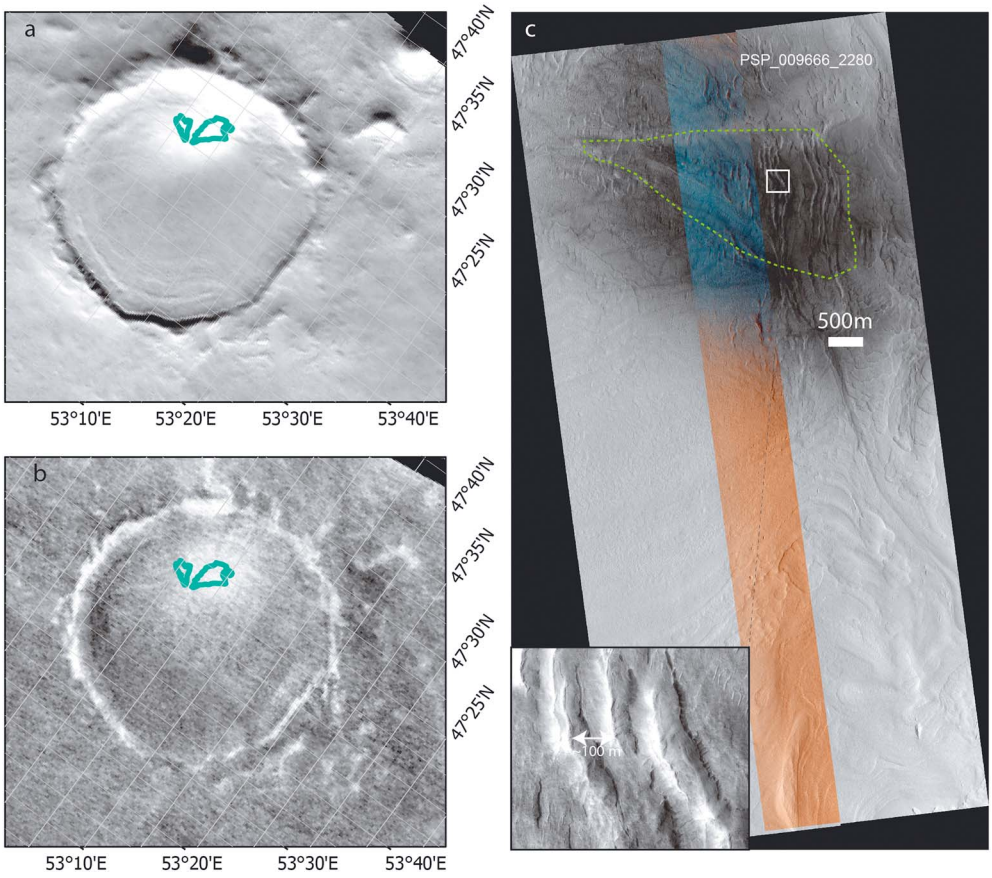

Figure 15. Context of the chlorite deposit in crater c194. (a) THEMIS daytime infrared image of crater c194 in Mars Polar Stereographic Projection; (b) THEMIS nighttime infrared image of the crater c194 in Mars North Polar Stereographic Projection, as a proxy for thermal inertia; (c) HiRISE image (PSP_009666_2280) of the ridged crater floor units of crater c194 showing the bluer-toned, relatively dust-free materials in HiRISE color with a zoomed-in window showing the ridged floor unit with chlorite detections. HiRISE = High Resolution Imaging Science Experiment; THEMIS = Thermal Emission Imaging System.

the impact. We focus, in particular, on the consequences of differential erosion of Lyot crater, the spatial distribution of hydrous minerals, and scenarios for the origin of prehnite to better constrain the formation conditions of hydrous minerals in both models.

5.2.1. The Differential Erosion of Lyot Crater

One confounding factor to interpreting the spatial distribution and geological context of hydrous minerals is the possibility of modification by later erosion and degradation. The crater shows asymmetric morphology between the southwest and the northeast sides (Figure 18). The raised rim of Lyot crater consists of a series of degraded knobs at varying elevations but is absent on the southwest side. The impact ring in the southwest is much lower in elevation than in the northeastern part of the crater. In addition, Lyot lacks an ejecta blanket and proximal secondary craters to the southwest, which could be due to the denudation of the southwestern rim, an oblique impact, or both (Robbins & Hynek, 2011; Russell & Head, 2002). The differential erosion may explain why less hydrous mineral detections are in the southwest part of the crater, while the northern and eastern rims of Lyot, where most hydrous minerals are found, are relatively well preserved.

The raised rim height for crater with a diameter of Lyot's is predicted to be 1.8–2.1 km relative to the preimpact surface (see section 3). Since there is large variation in the elevation of preimpact surface (−3.5 to −4.2 km) due to the northward downward trending slope of preimpact topography, we estimate the crater rim height by taking the MOLA elevation at the rim subtracted by the elevation immediately outside the continuous ejecta blanket in the same direction. Although heavily degraded, we find that the raised rim of Lyot can reach as high as ~1.7 km above the preimpact surface. We find that the height of Lyot's raised rim is close to the expected range. Prehnite deposits are mostly found at elevation above the preimpact surface, except when they occur in mass-wasting deposits (Figure 18). This suggests that the prehnite-bearing deposits are part of

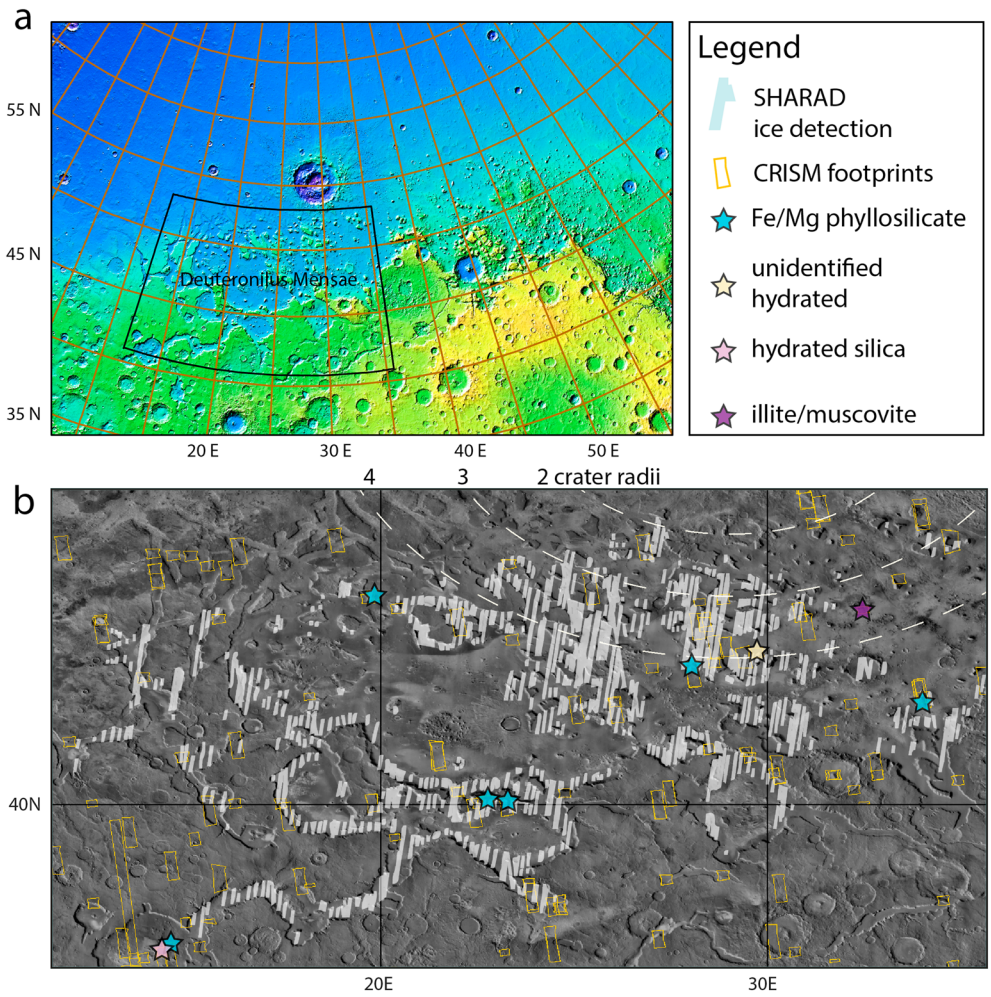

Figure 16. (a) Geological context map of Deuteronilus Mensae region, with MOLA color hillshade map in Mars North Polar Stereographic Projection. (b) SHARAD detection of subsurface ice (white stripes in the zoom image, personal correspondence from J. Plaut) in Deuteronilus Mensae south of Lyot with THEMIS day IR mosaic in the background. Also shown here are the CRISM footprints in this region and associated hydrous mineral detections. In relatively dust-free regions, small outcrops of Fe/Mg phyllosilicate, illite/muscovite, and unidentified hydrated minerals have been identified.
CRISM = Compact Reconnaissance Imaging Spectrometer for Mars; MOLA = Mars Orbiter Laser Altimeter; SHARAD = SHAllow RADar; THEMIS = Thermal Emission Imaging System.

the raised crater rim exposed after several hundred meters of erosion. Within the crater, the central peak and peak ring are the relatively low-lying topography, which is partially buried by the mantling unit.

5.2.2. Distribution of Hydrous Minerals in Lyot and Craters Nearby

The widespread hydrous mineralogy within Lyot crater shows at least five different spectral classes, which have been identified as follows: Fe/Mg smectite, chlorite, illite/muscovite, prehnite, and another hydrated mineral of unidentified type (see section 4.1). They mostly occur on or near the bedrock units in the central peak, peak ring, and terraced rim, even though the correlation to the morphology can be obscured due to mass wasting and denudation. The association with the bedrock units indicates formation directly related to the impact process, instead of transport, secondary sedimentation, or later weathering/alteration. The central peak of Lyot and the inner edge of crater peak ring are found with only unidentified hydrated detection and weak detections of Fe/Mg smectite, whereas prehnite, indicative of elevated temperature (>200 °C), is only found on the crater rim. Hydrous phases including chlorite and illite/muscovite are distributed between the peak ring and outer rim. We consider that impact melts may be preserved in Lyot crater and could give rise to some of the alteration signatures observed. However, due to the widespread mantling units of probably glacial origin (Dickson et al., 2009), this Amazonian-aged crater is more degraded than craters at lower latitudes, and impact melt deposits are not identified.

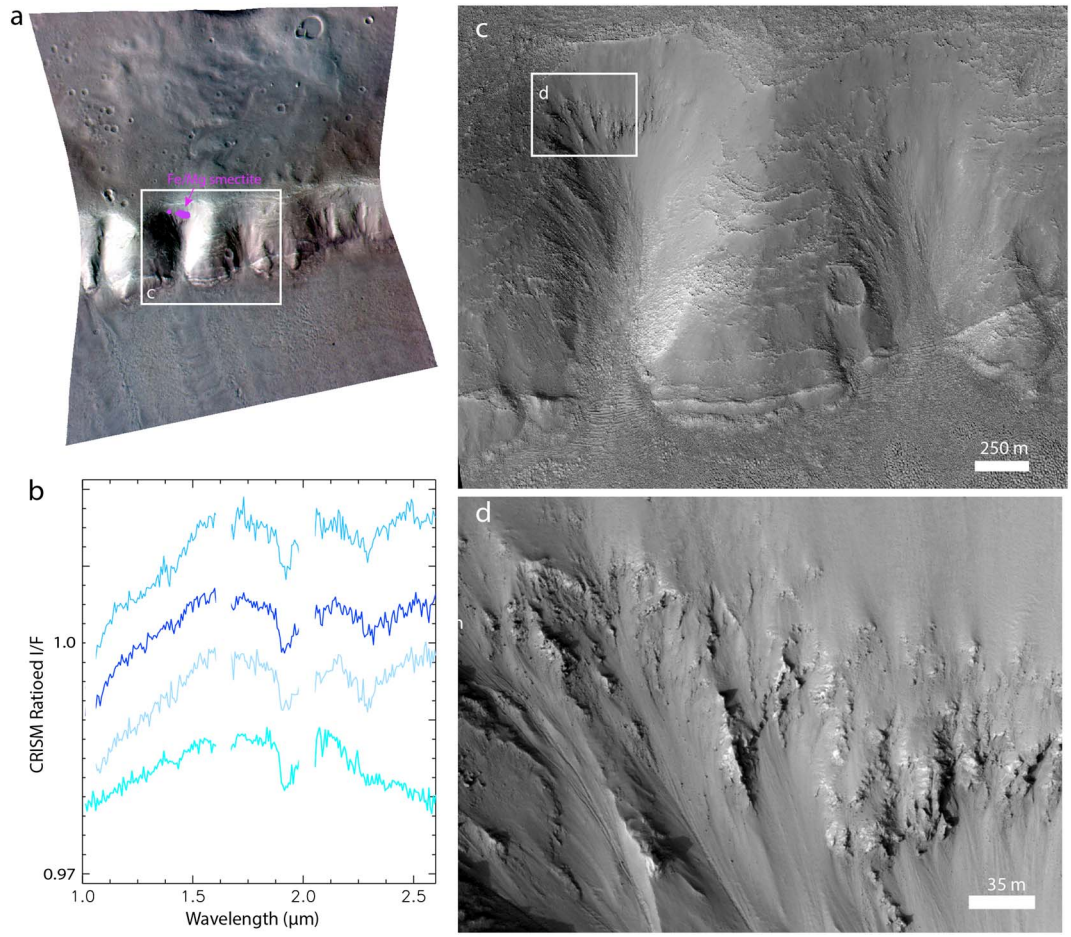

Figure 17. Exposure of phyllosilicate-bearing strata in Deuteronilus Mensae region. (a) CRISM image (FRT000049FF) of a southward facing scarp exposing Fe/Mg phyllosilicate. (b) Sample spectra from the highlighted region in (a) showing absorption bands at 1.9- and 2.3-μm region. (c and d) HiRISE image (PSP_002890_2205) of the outcrop, showing the bedrock on the scarp exposed due to active erosion.

The two craters to the west of Lyot (c308 and Micoud) show mineral assemblages similar to Lyot, while the other two craters (c308 and c394) have only chlorite associated with crater fill. The distribution and mineral assemblages found in Lyot, Micoud, and c308 are consistent with either excavation of the same preimpact altered stratigraphy or impact-induced hydrothermal alteration in similar geologic conditions. The existence of unaltered uplifted bedrock of mafic compositions (e.g., Figures 5, 12, and 13) in proximity with hydrous units can be explained by either excavation and mixing during the impact process or that any impact-induced alteration is limited to localized vents or cracks for aqueous solutions. The craters to the east of Lyot (c194 and c375) likely underwent a separate event where chlorite is either transported or formed in situ while the sediments formed within crater, which is spatially restricted to the east of Lyot crater.

5.2.3. Origin of Prehnite in Lyot and Micoud

Prehnite formation requires a temperature of 200–350 °C at low pressure (<3 kbar) and very low mole fraction of CO_2 ($XCO_2 << 0.1$; Robinson et al., 1999; Schiffman & Day, 1999), typically in association with chlorite and pumpellyite. In this study, we find a prehnite deposit on the east, northeast, and northwest side of the Lyot crater as well as in small patchy deposits in the central peak Micoud crater.

We first consider if the mineralogy and distribution of hydrous minerals in Lyot crater and its surroundings are consistent with the excavation of a hydrous-mineral-bearing subsurface stratigraphy. The various hydrous minerals could have formed in a subsurface stratigraphy if they have been buried since Noachian when the geothermal gradient was high enough for burial diagenesis. In the absence of a local heat source, typical hypothesized Noachian geotherms require at least 1.0–2.5 km of depth to reach the minimum temperature of typical chlorite/illite formation temperature (Borlina et al., 2015) and a minimum depth of ~5.5 km for prehnite formation.

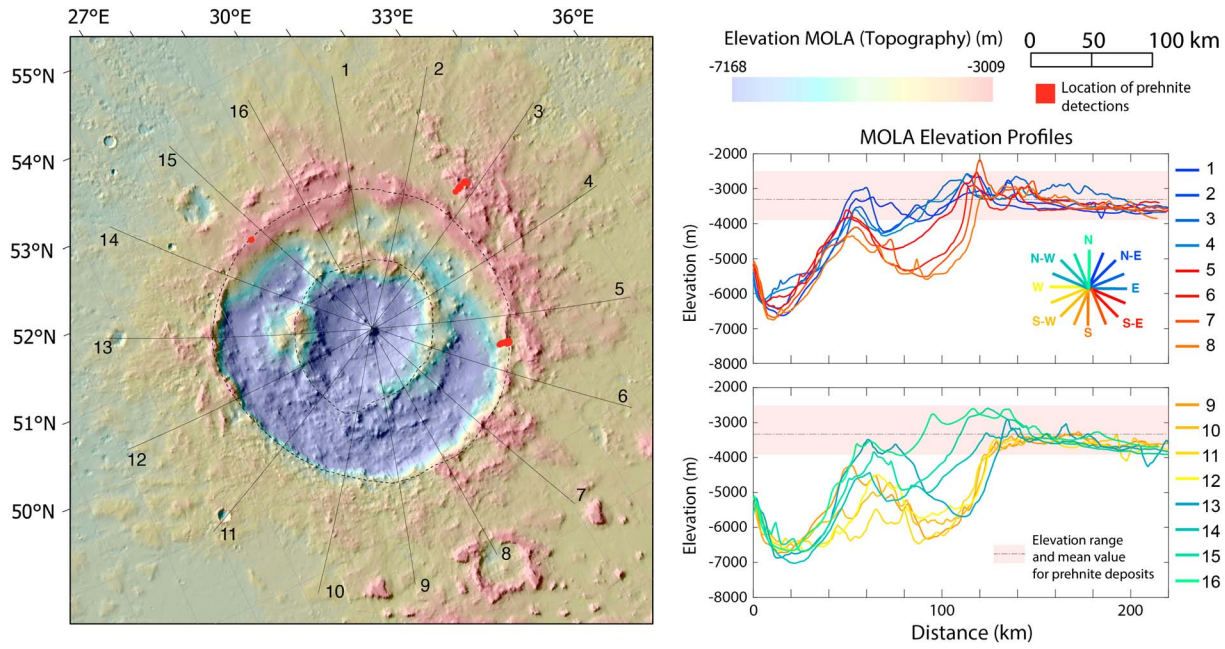

Figure 18. Topography map and cross sections of Lyot crater. Crater peak ring is lower in elevation and crater rim is more heavily degraded on the southwestern side (yellow-orange profiles). Black dashed lines highlight the locations of crater rim and crater ring. On the elevation profiles, pink shaded regions are the range of elevations of prehnite found in this study.

Although the maximum excavation depth of Lyot crater can reach 13–14 km, the collapsed crater rim is expected to originate from relatively shallow depths, as observed in similar-sized Chicxulub crater where the collapsed rim materials consist of sedimentary units originate from shallower than ~3 km depth (J. V. Morgan et al., 2016). The estimated structural uplift for Micoud crater central peak can reach ~4.9 km (Grieve & Pilkington, 1996). Based on these estimates, the original depth of prehnite should be less than 5 km deep, insufficient for the minimum depth required for prehnite formation. However, mixing of different lithologies occurs during the central peak formation (Kenkmann et al., 2014) and the development of reverse and normal faults on complex crater's terrace rim may induce kilometer-scale offsets of the original stratigraphy (Gulick, 2008), all inducing uncertainties to the original depth estimates. Thus, the formation of prehnite at depth cannot be completely ruled out but requires a higher geothermal gradient in the Noachian as proposed by Borlina et al. (2015). Otherwise, the relatively shallow original depth of prehnite would necessitate a locally elevated geothermal gradient or additional heat source preimpact for the formation of prehnite. Ancient impact or volcanic activity that mobilized subsurface water are both plausible scenarios for the formation of relatively shallow prehnite deposits.

In a syn-impact alteration scenario, both Lyot and Micoud craters are large enough to mobilize the subsurface cryosphere and sustain a hydrothermal system, though the heat source of the impact is predicted to be most intense at the center region when freezing is considered (Barnhart et al., 2010). In the central peak of Micoud crater, central peak temperatures are predicted to reach above 350 °C and thus may reach prehnite formation temperature postimpact (Abramov & Kring, 2005; Schwenzer et al., 2012). For Lyot crater, the crater floor and crater center do not have hydrous mineralogy indicative of elevated temperature, while the crater rim preserves such phases. The absence of prehnite in the central peak of Lyot may be due to the heterogeneity of the alteration or overprinting by cooler temperature alteration associated with the impact. The diagnostic petrologic textures that would preserve the evidence that impact heating facilitated the alteration or that the alteration predated the impact can only be seen at submeter scale. Future missions with the capability of resolving the microscale texture of the mineralogy may shed new light on the existence/absence of impact-induced hydrothermal systems on Mars.

5.3. Implications on Martian Climate in the Amazonian

As we have discussed, the observations of distribution of hydrous minerals within Lyot crater and its surroundings can be explained by impact excavation, syn-impact-induced alteration, or a combination of the two. Here we further discuss the implications for Martian climate based on these two endmembers.

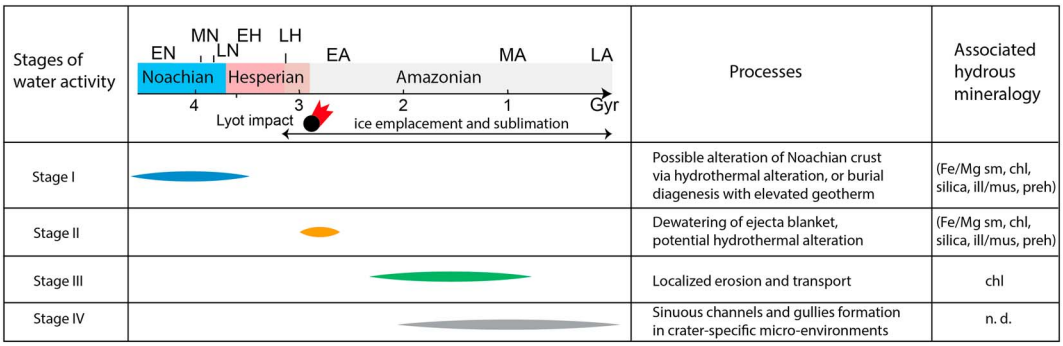

Figure 19. Timeline of different stages of aqueous activity in the Lyot vicinity, with possibly related hydrous mineralogy. Mars epoch boundaries are from the chronology by Hartmann and Neukum (2001). EN = Early Noachian; MN = Middle Noachian; LN = Late Noachian; EH = Early Hesperian; LH = Late Hesperian; EA = Early Amazonian; MA = Middle Amazonian; LA = Late Amazonian. Mineral abbreviations: chl = chlorite; Fe/Mg = Fe/Mg smectite; ill/mus = illite/muscovite; n.d. = not detected; preh = prehnite; silica = hydrated silica. Parentheses indicate minerals that are possibly related to a certain stage of water activity.

5.3.1. Excavation and Subsurface Origin of Lyot Minerals

The identification of diverse hydrous minerals associated with Lyot and its surroundings can be interpreted as the excavation of previous hydrous-mineral-bearing strata in the subsurface. In this scenario, the origin of these hydrous minerals is constrained to be early (Noachian-Hesperian). The formation of prehnite in relatively shallow depths involves an elevated heat flow near surface, either due to a locally elevated geothermal gradient or impact or volcanic activity preimpact. The hydrous mineral-bearing stratigraphy is later exposed by erosion and the energetic impact in the Early Amazonian, unrelated to the channel forming events either north of Lyot ejecta, or the small sinuous channels within Lyot crater.

5.3.2. Impact-Induced Hydrothermal Alteration

Alternatively, the impact could have mobilized liquid water to induce alteration during or immediately after the impact. In such a scenario, hydrous minerals may form via water/rock interactions during groundwater circulation, within impact melt vents, or from crystallization in impact melt glass (Tornabene et al., 2013). The impact-induced activity of the groundwater circulation in Lyot may have created localized environments with liquid water flow and enhanced alteration and could imply a cryosphere in the Lyot vicinity since the Early Amazonian. Nonetheless, the presence of prehnite detection on Lyot rim and the Micoud central peak and lack of detections in Lyot crater central peak suggest the secondary alteration in such a system is highly heterogeneous. The mafic blocks associated with hydrous minerals also indicate that the alteration is only restricted to regions where water may interact with bedrock locally, possibly through vents or fractures.

5.4. Synthesis of the Timeline of Aqueous Activity in Lyot Vicinity and Implications for Water on Amazonian Mars

From the investigation of mineralogy inside and surrounding Lyot crater, we suggest that the diverse hydrous minerals represent separate events of aqueous activity, predating geomorphic fluvial features found previously. Here we synthesize four possible stages of aqueous activity in the vicinity of Lyot constrained by the results of this study (Figure 19).

It is possible that some of the hydrous minerals, including Fe/Mg smectite, chlorite, and illite/muscovite, formed in the Noachian or Hesperian period via groundwater alteration, sometimes at hydrothermal/metamorphic temperatures, enabling the formation of prehnite. This may require elevated geotherm, the energy from previous impacts, or volcanic activity interacting with a local cryosphere or hydrologic cycle. As Lyot crater forms in the Early Amazonian, it either exposed the preimpact stratigraphy with diverse hydrous minerals or formed new aqueous alteration deposits from hydrothermal activity induced by the impact. Channeled scablands were created to the north of Lyot probably from dewatering of ejecta blanket or melting of the surface ice/snow (Harrison et al., 2010; Weiss et al., 2017). This channel-forming event was likely relatively short-lived and took place at low temperatures since it did not result in the formation of pervasive hydrous minerals.

Other small complex craters also formed nearby, some atop the Lyot ejecta blanket, excavating materials beneath. In the mid-late Amazonian, ice-related processes generate linear valley fills, lobate apron units, and mantling units, which were emplaced in the general region of Deuteronilus Mensae, extending to partially fill the craters in the vicinity of Lyot. Probably during this period, chlorite-bearing mantling materials are deposited within craters to the east of Lyot. These deposits are either comprised of transported materials or mineralized in situ by liquid water, for example, during burial diagenesis.

After the emplacement of the stippled mantling units in the Amazonian, localized channels formed in Lyot crater that cut across the stippled mantling units and are diverted by the preexisting topography with hydrous-mineral-bearing units. The lack of hydrous minerals associated the fluvial channels inside Lyot crater, which postdate the mantling units, indicates that during the period of formation of these geomorphic features related to liquid water activity, the surface water flow was transient in nature and/or mineral formation from water-rock interaction was kinetically inhibited, probably due to the low temperature of Mars surface.

6. Conclusions

The investigation into the mineralogical record of aqueous processes in Lyot and its surroundings revealed that smectite, chlorite, and illite/muscovite detections mostly occur within the crater peak ring and terraced crater rim, while prehnite units, indicative of formation temperature >200 °C, are found on the crater rim of

Table A1
Location of Spectral Detections in CRISM Data for Lyot and Small Craters

Figure #	Crater/region	Interpreted mineralogy	CRISM image ID	Center pixel/pixels	Number of pixels
2a	Lyot	Fe/Mg smectite	FRT0000CB40	X: 579 Y: 187	5 × 5
			FRT0000CB40	X: 41 Y: 341	5 × 5
			FRT0000CB40	X: 578 Y: 188	5 × 5
2b		Chlorite	FRT00020CC8	X: 588 Y: 99	7 × 7
			FRT00020CC8	X: 600 Y: 126	7 × 7
			FRT00018613	X: 366 Y: 277	5 × 5
			FRT0001721B	X: 594 Y: 63	6 × 6
2c		Illite/muscovite	FRS0003AEA3	X: 245 Y: 76	5 × 5
			FRT00020B25	X: 358 Y: 461	5 × 5
			FRT00020CC8	X: 247 Y: 218	7 × 7
			FRT00020CC8	X: 160 Y: 225	7 × 7
2d		Prehnite	FRS0002CB59	X: 382 Y: 116	5 × 5
			FRS000327E7	X: 373 Y: 148	5 × 5
2e		Unidentified	FRT0000CB40	X: 61 Y: 379	ROIs, 499
			FRT0000B133	X: 290 Y: 317	ROIs, 177
10a	c308	Fe/Mg smectite	FRT00017D51	X: 262 Y: 160	ROIs, 346
			FRT00017D51	X: 235 Y: 175, X: 238 Y:163	ROIs, 300
			FRT00017D51	X: 198 Y: 60	ROIs, 302
	Micoud	Fe/Mg smectite	FRT00016609	X: 543 Y: 61	5 × 5
			FRT00009C3C	X: 560 Y: 352	7 × 7
10b	Micoud	Chlorite	HRL0000C75D	X: 69 Y: 155	3 × 3
			HRL0000C75D	X: 142 Y: 309	3 × 3
	c194	Chlorite	FRT0000C141	X:240 Y: 313	5 × 5
			FRT0000C141	X: 233 Y: 321	5 × 5
	c375	Chlorite	FRT0000BFA6	X: 326 Y: 182	4 × 4
	Micoud	Unidentified	FRT00016609	X: 492 Y: 174	5 × 5
	c308	Unidentified	FRT00017D51	X: 204 Y: 234	7 × 7
10c	Micoud	Prehnite	HRL0000C75D	X: 147 Y: 279	3 × 3
			HRL0000C75D	X: 136 Y: 283	3 × 3
	Micoud	Illite/muscovite	HRL0000C75D	X: 231 Y: 207	5 × 5
			HRL0000C75D	X: 202 Y: 238	5 × 5
	c308	Hydrated silica	FRT00017D51	X: 325 Y: 191	ROIs, 302
17b	Deuteronilus Mensae	Fe/Mg phyllosilicate	FRT000049FF	X: 410 Y: 262	7 × 7
			FRT000049FF	X: 419 Y: 265	7 × 7
			FRT000049FF	X: 427 Y: 267	7 × 7
			FRT000049FF	X: 443 Y: 270	7 × 7

Note. CRISM = Compact Reconnaissance Imaging Spectrometer for Mars.

Lyot. The hydrous minerals in smaller craters to the west of Lyot are similar to those found within Lyot crater while the two craters to the east of Lyot (c395 and c194) are filled with later mantling deposits.

The hydrous minerals in Lyot may be explained by the excavation of a preimpact stratigraphy with burial diagenesis or an episode of hydrothermal alteration having occurred in the Noachian or Hesperian, due to an earlier impact or volcanic activity providing external heat source. Alternatively, they may indicate heterogeneous alteration of the exposed bedrock immediately after the impact in the Amazonian. The hydrous minerals in smaller complex craters probably represent similar process of excavation and/or postimpact alteration with similar subsurface strata or similar conditions during the impact. The chlorite deposits within the crater fill units could have been transported from elsewhere or locally mineralized postimpact.

No evidence of hydrous minerals was found in association with ice deposits nearby in Deuteronilus Mensae nor within the previously identified channeled scablands to the north of Lyot, which emanate from the ejecta blanket and likely formed from impact heating of ice-rich materials. Sinuous, fluvial channels within Lyot formed in a still later stage of aqueous activity, which clearly postdates the emplacement of the hydrous-mineral-bearing knobs. The lack of hydrous mineralization in association with the fluvial channels indicates that localized liquid water activity was present in the later Amazonian, and may still occur, but that mineralization was inhibited by short durations or cold temperatures as appears to be the case over most of Amazonian Mars.

Appendix A

Following the methods described in section 3, the spectral data and mineral maps can be reproduced with the information in this appendix. For all CRISM detections shown in Figures 2–17, we provide CRISM image IDs, coordinates of the center point, and the size of the regions of interest where the CRISM spectra are extracted (Table A1). Image IDs, projection, and spectral parameters for reproducing spectral parameter maps and color overlays in Figures 2–15 are given in Table A2. We also list CRISM images investigated north of Lyot crater (Table A3) and in the Deuteronilus Mensae region (Table A4).

Table A2
Details on CRISM spectral parameter maps and color overlays with HiRISE and CTX

Figure #	Crater	Interpreted hydrous mineralogy	CRISM image ID	Base image	Projection	Spectral parameters
5	Lyot	Fe/Mg smectite	FRT0000CB40	CTX: D02_027864_2294_XN_49N330W	Mars North Polar Stereographic Projection	R: BD(Olivine) G: BD(1.9μm) B: BD(Mg-OH)
6	Lyot	chlorite, illite/muscovite, prehnite	FRT00020B25	CTX: D19_034602_2296_XN_49N328W	Simple Cylindrical	R: BD(1.9μm) G: BD(Mg-OH) B: BD(2.35μm)
7a	Lyot	chlorite, illite/muscovite	FRT00020B25	CTX mosaic	Mars North Polar Stereographic Projection	mapping based on BD(Mg-OH) & BD(2.35μm)
7b	Lyot	chlorite-smectite	FRT00023F1F	CTX mosaic	Mars North Polar Stereographic Projection	mapping based on BD(Mg-OH) & BD(2.35μm)
7c	Lyot	illite/muscovite	FRT00021FCB	CTX mosaic	Mars North Polar Stereographic Projection	mapping based on BD(Mg-OH) & BD(2.35μm)
8	Lyot	prehnite, chlorite	FRS0002CB59, FRT00020B25	CTX: D19_034602_2296_XN_49N328W	Simple Cylindrical	mapping based on BD(Mg-OH) & BD(2.35μm)
9	Lyot	unidentified	FRT0000B133	HiRISE: ESP_027376_2310	Simple Cylindrical	mapping based on BD(1.9μm)
12	Micoud	chlorite, prehnite, illite/muscovite, unidentified	FRT00019658	HiRISE: PSP_009997_2310	Simple Cylindrical	R: BD(1.9μm) G: BD(Al-OH) B: BD(Mg-OH)
13	c308	Fe/Mg smectite, hydrated silica	FRT00017D41	HiRISE: ESP_025082_2295	Simple Cylindrical	mapping based on spectral parameters BD(1.9μm), BD(Mg-OH) & BD(Al-OH)
14b	c375	chlorite	FRT0000BFA6	HiRISE: ESP_044149_2325	Simple Cylindrical	R: BD (Olivine) G: BD (1.9μm) B: BD (Mg-OH)
15c	c194	chlorite	FRT0000C141	PSP_009666_2280	Simple Cylindrical	mapping based on BD (2.3μm)

Note. HiRISE = High Resolution Imaging Science Experiment; CRISM = Compact Reconnaissance Imaging Spectrometer for Mars; CTX = Context Camera.

Table A3
List of CRISM images covering channels north of Lyot

Day of year	CRISM_ID	Lat	Lon
2013_281	FRS0002BB47	65.0	31.2
2014_202	FRS00031515	55.2	27.3
2014_203	FRS0003156A	57.3	32.0
2014_251	FRS0003278F	55.2	27.3
2015_242	FRS00037F56	55.3	20.4
2015_243	FRS00037F8F	55.2	27.3
2015_347	FRS000396CF	55.3	20.4
2015_359	FRS000399AD	55.2	27.3
2008_004	FRT0000931B	59.0	32.1
2008_015	FRT0000972C	64.9	31.3
2008_055	FRT0000A15B	64.8	31.6
2008_121	FRT0000AAA1	64.9	31.2
2008_131	FRT0000AC4F	61.6	21.9
2008_167	FRT0000B188	64.9	31.2
2008_204	FRT0000BB16	58.2	23.2
2008_299	FRT0000D178	64.9	31.2
2008_316	FRT0000D522	64.9	31.2
2010_074	FRT00017391	56.3	24.4
2010_075	FRT000173ED	59.2	28.0
2010_080	FRT000175C1	56.7	27.7
2010_081	FRT0001762D	56.0	33.8
2010_129	FRT00018AE9	61.0	24.2
2010_130	FRT00018B41	60.8	29.6
2012_061	FRT000235DB	61.5	21.9
2012_100	FRT00024453	61.5	21.9
2008_194	HRL0000B815	64.9	31.2
2008_291	HRL0000CFAC	57.9	19.8
2008_002	HRS0000926E	63.5	20.8
2009_196	HRS00013BBA	63.5	21.5
2010_103	HRS00017E89	56.5	21.2
2010_133	HRS00018C43	57.8	18.7
2010_142	HRS00018EED	62.9	35.9

Note. CRISM = Compact Reconnaissance Imaging Spectrometer for Mars.

Table A4
List of CRISM Images in the Deuteronilus Mensae Region

Day of year	CRISM_ID	Lat	Lon	Hydrous mineralogy interpretation
2008_125	HRS0000AB71	45.2	28.2	
2008_232	HRS0000C183	45.0	32.5	Illite/muscovite or prehnite
2007_302	FRT0000882E	45.8	33.4	
2007_363	FRT00009101	42.6	32.2	
2008_001	FRT00009213	45.3	19.7	
2008_026	FRT00009A54	46.8	32.1	
2008_040	FRT00009DA4	45.1	20.4	
2008_041	FRT00009DEC	42.6	26.1	
2008_042	FRT00009E2C	47.3	31.2	
2008_120	FRT0000AA76	43.9	29.7	hydrated unidentified
2008_064	FRT0000A3D1	43.6	27.0	
2008_181	FRT0000B47C	44.3	23.4	
2010_040	FRT00016665	44.4	45.0	
2008_172	HRL0000B29B	42.3	42.9	
2008_221	HRL0000BF50	43.3	44.0	
2008_249	HRL0000C58E	49.7	50.4	
2009_053	HRL000113FF	44.1	28.9	
2012_309	FRS0002749B	44.7	30.9	
2015_236	FRS00037DBB	45.3	19.8	Fe/Mg phyllosilicate

Table A4 *(continued)*

Day of year	CRISM_ID	Lat	Lon	Hydrous mineralogy interpretation
2016_326	FRS0003E1D4	43.3	27.6	
2016_242	FRS0003E3C1	43.4	30.4	
2007_068	FRT000049FF	40.1	22.8	Fe/Mg phyllosilicate
2007_263	FRT00007CC5	40.8	32.9	
2007_300	FRT00008780	37.3	24.6	
2007_362	FRT000090A0	38.2	28.9	
2008_008	FRT00009486	41.2	29.6	
2008_020	FRT000098A6	41.3	29.5	
2008_058	FRT0000A230	40.3	24.8	
2008_060	FRT0000A2B9	35.8	34.8	
2008_110	FRT0000A893	40.6	34.9	
2008_199	FRT0000B9DA	37.5	34.6	
2007_106	HRL00005685	32.6	21.3	
2008_057	HRL0000A1EF	40.0	19.8	
2008_124	HRL0000AB4C	37.3	24.5	
2008_219	HRL0000BEF4	39.9	23.2	Fe/Mg phyllosilicate
2008_225	HRL0000C001	37.4	24.7	
2009_086	HRL00011C8F	34.4	29.6	
2009_091	HRL00011D77	36.5	27.2	
2011_100	HRL0001DA90	36.6	24.4	
2008_002	HRS0000926D	35.5	26.4	
2009_109	HRS000121F3	35.0	32.5	
2009_118	HRS00012529	36.2	23.2	
2009_196	HRS00013BB9	35.5	27.0	
2010_343	HRS0001C567	39.2	20.4	
2012_288	FRS0002702B	42.7	34.0	Fe/Mg phyllosilicate
2012_304	FRS00027387	42.7	34.0	Fe/Mg phyllosilicate
2012_308	FRS0002745D	40.0	27.5	
2014_085	FRS0002EC9D	37.8	23.9	
2014_086	FRS0002ED05	41.4	28.5	
2014_092	FRS0002EF6C	36.0	31.8	
2014_255	FRS000328AD	37.9	18.2	
2015_099	FRS00036403	40.7	30.2	
2015_353	FRS00039848	35.5	26.3	
2016_130	FRS0003BF58	35.8	23.9	
2016_179	FRS0003CFDE	38.9	22.7	
2016_180	FRS0003D03F	36.6	26.7	
2016_190	FRS0003D372	37.8	23.9	
2013_284	FRS0002BBA0	36.9	37.0	
2014_094	FRS0002EFF3	36.9	15.0	
2007_116	FRT00005A4D	36.3	15.3	
2007_365	FRT000091C0	46.4	15.1	
2008_017	FRT00009794	46.5	14.1	
2008_062	FRT0000A345	46.2	15.5	
2008_190	FRT0000B6B0	40.0	16.2	
2008_240	FRT0000C380	36.2	14.3	Fe/Mg phyllosilicate, hydrated silica
2009_015	FRT000108AD	40.8	31.7	
2009_017	FRT00010932	44.8	15.8	
2009_019	FRT000109A8	38.0	27.4	
2009_114	FRT000123B0	36.2	30.7	
2009_169	FRT000134CC	40.7	31.7	
2009_181	FRT000136C5	40.4	32.2	
2009_206	FRT00013F15	40.0	22.5	
2010_044	FRT000167CD	46.1	14.2	
2010_045	FRT0001682D	40.3	22.0	
2010_052	FRT00016B62	45.3	28.9	
2010_056	FRT00016D34	40.3	22.0	
2010_058	FRT00016E1B	41.9	31.6	
2010_068	FRT000171BF	43.7	28.6	
2010_085	FRT000177AC	44.7	28.4	
2010_099	FRT00017CF2	40.0	17.4	

Table A4 *(continued)*

Day of year	CRISM_ID	Lat	Lon	Hydrous mineralogy interpretation
2010_307	FRT0001BAA5	47.8	31.4	
2011_355	FRT00021F9D	43.6	28.0	Fe/Mg phyllosilicate
2012_056	FRT0002340C	40.2	27.2	
2012_088	FRT00024094	41.5	21.5	
2012_092	FRT000241F0	36.3	14.5	Fe/Mg phyllosilicate, hydrated silica
2012_098	FRT000243C9	38.2	18.0	
2012_111	FRT00024794	41.1	30.2	
2012_126	FRT00024C2D	41.5	21.5	
2008_050	HRL0000A061	46.1	16.0	
2010_124	HRL00018895	44.7	28.4	
2011_229	HRL0001FBF1	48.1	31.0	
2010_183	HRS000199D2	42.7	18.2	

Note. CRISM = Compact Reconnaissance Imaging Spectrometer for Mars.

Acknowledgments
All the imagery data presented in this work are archived on the Planetary Data System (https://pds.nasa.gov/). We acknowledge funding from NASA Mars Data Analysis Program grant NNX12AJ43G to B. L. E. and from the European Union's Horizon 2020 research and innovation program under the Marie Sklodowska-Curie grant agreement 751164 to L. P. The manuscript was greatly enhanced by reviews from L. Ojha and an anonymous reviewer. We thank the CRISM team for targeting and providing the data set. We would also like to thank Jeffrey Plaut for sharing the map for SHARAD ice detection in Deuteronilus Mensae, and Jay Dickson for the help in processing the CTX mosaic.

References

Abramov, O., & Kring, D. A. (2005). Impact-induced hydrothermal activity on early Mars. *Journal of Geophysical Research*, *110*, E12S09. https://doi.org/10.1029/2005JE002453

Allen, C. C., Gooding, J. L., & Keil, K. (1982). Hydrothermally altered impact melt rock and breccia: Contributions to the soils of Mars. *Journal of Geophysical Research*, *87*, 10,083–10,101. https://doi.org/10.1029/JB087iB12p10083

Anderson, J. H., & Wickersheim, K. A. (1964). Near infrared characterization of water and hydroxyl groups on silica surfaces. *Surface Science*, *2*, 252–260. https://doi.org/10.1016/0039-6028(64)90064-0

Baker, D. M. H., & Carter, L. M. (2017). Radar reflectors associated with an ice-rich mantle unit in Deuteronilus Mensae, Mars, Lunar and Planetary Science Conference XLVII, vol. 1575.

Baker, D. M. H., Head, J. W., & Marchant, D. R. (2010). Flow patterns of lobate debris aprons and lineated valley fill north of Ismeniae Fossae, Mars: Evidence for extensive mid-latitude glaciation in the Late Amazonian. *Icarus*, *207*(1), 186–209. https://doi.org/10.1016/j.icarus.2009.11.017

Barnhart, C. J., Nimmo, F., & Travis, B. J. (2010). Martian post-impact hydrothermal systems incorporating freezing. *Icarus*, *208*(1), 101–117. https://doi.org/10.1016/j.icarus.2010.01.013

Bibring, J.-P., Langevin, Y., Mustard, J. F., Poulet, F., Arvidson, R., Gendrin, A., et al. (2006). Global mineralogical and aqueous Mars history derived from OMEGA/Mars Express Data. *Science*, *312*(5772), 400–404. https://doi.org/10.1126/science.1122659

Bishop, J., Madejová, J., Komadel, P., & Fröschl, H. (2002). The influence of structural Fe, Al and Mg on the infrared OH bands in spectra of dioctahedral smectites. *Clay Minerals*, *37*(4), 607–616. https://doi.org/10.1180/0009855023740063

Bishop, J. L., Lane, M. D., Dyar, M. D., & Brown, A. J. (2008). Reflectance and emission spectroscopy study of four groups of phyllosilicates: Smectites, kaolinite-serpentines, chlorites and micas. *Clay Minerals*, *43*(1), 35–54. https://doi.org/10.1180/claymin.2008.043.1.03

Borlina, C. S., Ehlmann, B. L., & Kite, E. S. (2015). Modeling the thermal and physical evolution of Mount Sharp's sedimentary rocks, Gale crater, Mars: Implications for diagenesis on the MSL Curiosity rover traverse. *Journal of Geophysical Research: Planets*, *120*, 1396–1414. https://doi.org/10.1002/2015JE004799

Brakenridge, G. R., Newsom, H. E., & Baker, V. R. (1985). Ancient hot springs on Mars: Origins and paleoenvironmental significance of small Martian valleys. *Geology*, *13*(12), 859–862. https://doi.org/10.1130/0091-7613(1985)13%3C859:AHSOMO%3E2.0.CO;2

Byrne, S., Dundas, C. M., Kennedy, M. R., Mellon, M. T., McEwen, A. S., Cull, S. C., et al. (2009). Distribution of mid-latitude ground ice on mars from new impact craters. *Science*, *325*(5948), 1674–1676. https://doi.org/10.1126/science.1175307

Carter, J., Poulet, F., Bibring, J. P., Mangold, N., & Murchie, S. (2013). Hydrous minerals on Mars as seen by the CRISM and OMEGA imaging spectrometers: Updated global view. *Journal of Geophysical Research: Planets*, *118*, 831–858. https://doi.org/10.1029/2012JE004145

Carter, J., Poulet, F., Bibring, J.-P., & Murchie, S. (2010). Detection of hydrated silicates in crustal outcrops in the northern plains of Mars. *Science*, *328*(5986), 1682–1686. https://doi.org/10.1126/science.1189013

Christensen, P. R., Jakosky, B. M., Kieffer, H. H., Malin, M. C., McSween, Jr, H. Y., Nealson, K., et al. (2004). The Thermal Emission Imaging System (THEMIS) for the Mars 2001 Odyssey Mission. *Space Science Reviews*, *110*(1/2), 85–130. https://doi.org/10.1023/B:SPAC.0000021008.16305.94

Clark, R. N. (1999). Spectroscopy of rocks and minerals, and principles of spectroscopy. In A. N. Rencz (Ed.), *Remote sensing for the earth sciences: Manual of remote sensing* (3rd ed., pp. 3–58). New York: John Wiley. https://doi.org/10.1111/j.1945-5100.2004.tb00079.x

Clark, R. N., King, T. V. V., Klejwa, M., Swayze, G. A., & Vergo, N. (1990). High spectral resolution reflectance spectroscopy of minerals. *Journal of Geophysical Research*, *95*, 12,653–12,680. https://doi.org/10.1029/JB095iB08p12653

Clark, R. N., Swayze, G. A., Wise, R., Livo, E., Hoefen, T., Kokaly, R., & Sutley, S. J. (2007). USGS digital spectral library splib06a, U.S. Geological Survey, Digital Data Series 231. Retrieved from http://speclab.cr.usgs.gov/spectral.lib06

Clifford, S. M. (1993). A model for the hydrologic and climatic behavior of water on Mars. *Journal of Geophysical Research*, *98*, 10,973–11,016. https://doi.org/10.1029/93JE00225

Clifford, S. M., & Parker, T. J. (2001). The evolution of the Martian hydrosphere: Implications for the fate of a Primordial Ocean and the current state of the Northern Plains. *Icarus*, *154*(1), 40–79. https://doi.org/10.1006/icar.2001.6671

Croft, S. (1985). The scaling of complex craters. *Journal of Geophysical Research*, *90*, C828–C842. https://doi.org/10.1029/JB090iS02p0C828

Dickson, J. L., Fassett, C. I., & Head, J. W. (2009). Amazonian-aged fluvial valley systems in a climatic microenvironment on Mars: Melting of ice deposits on the interior of Lyot crater. *Geophysical Research Letters*, *36*, L08201. https://doi.org/10.1029/2009GL037472

Dickson, J. L., Head, J. W., & Marchant, D. R. (2008). Late Amazonian glaciation at the dichotomy boundary on Mars: Evidence for glacial thickness maxima and multiple glacial phases. *Geology*, *36*(5), 411–414. https://doi.org/10.1130/G24382A.1

Dickson, J. L., Kerber, L. A., Fassett, C. I., & Ehlmann, B. L. (2018). A Global, Blended CTX Mosaic of Mars with Vectorized Seam Mapping: A New Mosaicking Pipeline Using Principles of Non-Destructive Image Editing. In *Lunar and Planetary Science Conference* (Vol. 49, pp. 1–2).

Dundas, C. M., Bramson, A. M., Ojha, L., Wray, J. J., Mellon, M. T., Byrne, S., et al. (2018). Exposed subsurface ice sheets in the Martian mid-latitudes. *Science*, *359*(6372), 199–201. https://doi.org/10.1126/science.aao1619

Edwards, C. S., Nowicki, K. J., Christensen, P. R., Hill, J., Gorelick, N., & Murray, K. (2011). Mosaicking of global planetary image datasets: 1. Techniques and data processing for Thermal Emission Imaging System (THEMIS) multi-spectral data. *Journal of Geophysical Research*, *116*, E10005. https://doi.org/10.1029/2010JE003755

Ehlmann, B. L., & Edwards, C. S. (2014). Mineralogy of the Martian surface. *Annual Review of Earth and Planetary Sciences*, *42*(1), 291–315. https://doi.org/10.1146/annurev-earth-060313-055024

Ehlmann, B. L., Mustard, J. F., Murchie, S. L., Bibring, J. P., Meunier, A., Fraeman, A. A., & Langevin, Y. (2011). Subsurface water and clay mineral formation during the early history of Mars. *Nature*, *479*(7371), 53–60. https://doi.org/10.1038/nature10582

Ehlmann, B. L., Mustard, J. F., Swayze, G. A., Clark, R. N., Bishop, J. L., Poulet, F., et al. (2009). Identification of hydrated silicate minerals on Mars using MRO-CRISM: Geologic context near Nili Fossae and implications for aqueous alteration. *Journal of Geophysical Research*, *114*, E00D08. https://doi.org/10.1029/2009JE003339

Fassett, C. I., Dickson, J. L., Head, J. W., Levy, J. S., & Marchant, D. R. (2010). Supraglacial and proglacial valleys on Amazonian Mars. *Icarus*, *208*(1), 86–100. https://doi.org/10.1016/j.icarus.2010.02.021

Fraeman, A. A., Mustard, J. F., Ehlmann, B. L., Roach, L. H., Milliken, R. E., Murchie, S. L. (2009). Evaluating models of crustal cooling using CRISM observations of impact craters in Terra Tyrrhena and Noachis Terra, Lunar Planet. Sci., XL, Abstract 2320.

Frey, H. V. (2002). Ancient lowlands on Mars. *Geophysical Research Letters*, *29*(10), 1384. https://doi.org/10.1029/2001GL013832

Gaffey, S. J. (1987). Spectral reflectance of carbonate minerals in the visible and near infrared (0.35-2.55um): Anhydrous Carbonate Minerals. *Journal of Geophysical Research*, *92*(B2), 1429–1440.

Garvin, J. B., & Frawley, J. J. (1998). Geometric properties of Martian impact craters: Preliminary results from the Mars Orbiter Laser Altimeter. *Geophysical Research Letters*, *25*(24), 4405–4408. https://doi.org/10.1029/1998GL900177

Garvin, J. B., Sakimoto, S. E. H., & Frawley, J. J. (2003). Craters on Mars: Global geometric properties from gridded MOLA topography, Sxith Int. Conf. Mars, 7–9.

Grieve, R. A. F., & Pilkington, M. (1996). The signature of terrestrial impacts. *AGSO Journal of Australian Geology and Geophysics*, *13*(4), 61–420. https://doi.org/10.2307/270718

Gulick, S. P. S. (2008). Importance of pre-impact crustal structure for the asymmetry of the Chicxulub impact crater. *Nature Geoscience*, *1*(2), 131–135. https://doi.org/10.1038/ngeo103

Harrison, T. N., Malin, M. C., Edgett, K. S., Shean, D. E., Kennedy, M. R., Lipkaman, L. J., et al. (2010). Impact-induced overland fluid flow and channelized erosion at Lyot crater, Mars. *Geophysical Research Letters*, *37*, L21201. https://doi.org/10.1029/2010GL045074

Hartmann, W. K., & Neukum, G. (2001). Cratering chronology and the evolution of Mars. *Space Science Reviews*, *96*(1/4), 165–194. https://doi.org/10.1023/A:1011945222010

Head, J., Mustard, J., Kreslavsky, M., Milliken, R., & Marchant, D. (2003). Recent ice ages on Mars. *Nature*, *426*(6968), 797–802. https://doi.org/10.1038/nature02114

Head, J. W., Nahm, A. L., Marchant, D. R., & Neukum, G. (2006). Modification of the dichotomy boundary on Mars by Amazonian mid-latitude regional glaciation. *Geophysical Research Letters*, *33*, L08S03. https://doi.org/10.1029/2005GL024360

Holsapple, K. A. (1993). The scaling of impact processes in planetary sciences. *Annual Review of Earth and Planetary Sciences*, *21*, 333–373. https://doi.org/10.1146/annurev.ea.21.050193.002001

Jones, A. P., McEwen, A. S., Tornabene, L. L., Baker, V. R., Melosh, H. J., & Berman, D. C. (2011). A geomorphic analysis of Hale crater, Mars: The effects of impact into ice-rich crust. *Icarus*, *211*(1), 259–272. https://doi.org/10.1016/j.icarus.2010.10.014

Kenkmann, T., Poelchau, M. H., & Wulf, G. (2014). Structural geology of impact craters. *Journal of Structural Geology*, *62*, 156–182. https://doi.org/10.1016/j.jsg.2014.01.015

Levy, J., Head, J. W., & Marchant, D. R. (2010). Concentric crater fill in the northern mid-latitudes of Mars: Formation processes and relationships to similar landforms of glacial origin. *Icarus*, *209*(2), 390–404. https://doi.org/10.1016/j.icarus.2010.03.036

Levy, J. S., Head, J. W., & Marchant, D. R. (2007). Lineated valley fill and lobate debris apron stratigraphy in Nilosyrtis Mensae, Mars: Evidence for phases of glacial modification of the dichotomy boundary. *Journal of Geophysical Research*, *112*, E08004. https://doi.org/10.1029/2006JE002852

Lucchitta, B. K. (1984). Ice and debris in the fretted terrain, Mars. *Journal of Geophysical Research*, *89*, B409–B418. https://doi.org/10.1029/JB089iS02p0B409

Lucchitta, K., & Earth, O. (1981). Mars and Earth: Comparison of Cold-Climate Features. *Icarus*, *303*, 264–303.

Malin, M. C., Bell, J. F. III, Cantor, B. A., Caplinger, M. A., Calvin, W. M., Clancy, R. T., et al. (2007). Context Camera investigation on board the Mars Reconnaissance Orbiter. *Journal of Geophysical Research*, *112*, E05S04. https://doi.org/10.1029/2006JE002808

Malin, M. C., & Edgett, K. S. (2000). Evidence for recent groundwater seepage and surface runoff on Mars. *Science*, *288*(5475), 2330–2335. https://doi.org/10.1126/science.288.5475.2330

Mangold, N., Carter, J., Poulet, F., Dehouck, E., Ansan, V., & Loizeau, D. (2012). Late Hesperian aqueous alteration at Majuro crater, Mars. *Planetary and Space Science*, *72*(1), 18–30. https://doi.org/10.1016/j.pss.2012.03.014

Marzo, G. A., Roush, T. L., Lanza, N. L., McGuire, P. C., Newsom, H. E., Ollila, A. M., & Wiseman, S. M. (2009). Association of phyllosilicates and the inverted channel in Miyamoto crater, Mars. *Geophysical Research Letters*, *36*, L11204. https://doi.org/10.1029/2009GL038703

McEwen, A. S., Eliason, E. M., Bergstrom, J. W., Bridges, N. T., Hansen, C. J., Delamere, W. A., et al. (2007). Mars Reconnaissance Orbiter's High-Resolution Imaging Science Experiment (HiRISE). *Journal of Geophysical Research*, *112*, E05S02. https://doi.org/10.1029/2005JE002605

McEwen, A. S., Hansen, C. J., Delamere, W. A., Eliason, E. M., Herkenhoff, K. E., Keszthelyi, L., et al. (2007). A closer look at water-related geologic activity on Mars. *Science*, *317*(5845), 1706–1709. https://doi.org/10.1126/science.1143987

McEwen, A. S., Ojha, L., Dundas, C. M., Mattson, S. S., Byrne, S., Wray, J. J., et al. (2011). Seasonal flows on warm Martian slopes. *Science*, *333*(6043), 740–743. https://doi.org/10.1126/science.1204816

Mellon, M. T., & Phillips, R. J. (2001). Recent gullies on Mars and the source of liquid water. *Journal of Geophysical Research*, *106*, 23,165–23,179. https://doi.org/10.1029/2000JE001424

Melosh, H. J. (1989). Impact Cratering: A Geologic Process, Res. Oxford Univ. Press No. 11 1989 46 p, 49 (14–15), 245. https://doi.org/10.1103/PhysRevB.46.10411

Milliken, R. E., Swayze, G. A., Arvidson, R. E., Bishop, J. L., Clark, R. N., Ehlmann, B. L., et al. (2008). Opaline silica in young deposits on Mars. *Geology*, *36*(11), 847–850. https://doi.org/10.1130/G24967A.1
Morgan, G. A., & Head, J. W. (2009). Sinton crater, Mars: Evidence for impact into a plateau icefield and melting to produce valley networks at the Hesperian-Amazonian boundary. *Icarus*, *202*(1), 39–59. https://doi.org/10.1016/j.icarus.2009.02.025
Morgan, G. A., Head, J. W., & Marchant, D. R. (2009). Lineated valley fill (LVF) and lobate debris aprons (LDA) in the Deuteronilus Mensae northern dichotomy boundary region, Mars: Constraints on the extent, age and episodicity of Amazonian glacial events. *Icarus*, *202*(1), 22–38. https://doi.org/10.1016/j.icarus.2009.02.017
Morgan, J. V., Gulick, S. P. S., Bralower, T., Chenot, E., Christeson, G., Claeys, P., et al. (2016). The formation of peak rings in large impact craters. *Science*, *354*(6314), 878–882. https://doi.org/10.1126/science.aah6561
Morgan, J. V., Warner, M. R., Collins, G. S., Melosh, H. J., & Christeson, G. L. (2000). Peak-ring formation in large impact craters: Geophysical constraints from Chicxulub. *Earth and Planetary Science Letters*, *183*, 347–354.
Murchie, S., Arvidson, R., Bedini, P., Beisser, K., Bibring, J. P., Bishop, J., et al. (2007). Compact Connaissance Imaging Spectrometer for Mars (CRISM) on Mars Reconnaissance Orbiter (MRO). *Journal of Geophysical Research*, *112*, E05S03. https://doi.org/10.1029/2006JE002682
Murchie, S. L., Seelos, F. P., Hash, C. D., Humm, D. C., Malaret, E., McGovern, J. A., et al. (2009). Compact Reconnaissance Imaging Spectrometer for Mars investigation and data set from the Mars Reconnaissance Orbiter's primary science phase. *Journal of Geophysical Research*, *114*, E00D07. https://doi.org/10.1029/2009JE003344
Mustard, J. F., Cooper, C. D., & Rifkin, M. K. (2001). Evidence for recent climate change on Mars from the identification of youthful near-surface ground ice. *Nature*, *412*(6845), 411–414. https://doi.org/10.1038/35086515
Mustard, J. F., Murchie, S. L., Pelkey, S. M., Ehlmann, B. L., Milliken, R. E., Grant, J. A., et al. (2008). Hydrated silicate minerals on Mars observed by the Mars Reconnaissance Orbiter CRISM instrument. *Nature*, *454*(7202), 305–309. https://doi.org/10.1038/nature07097
Naumov, M. V. (2005). Principal features of impact-generated hydrothermal circulation systems: Mineralogical and geochemical evidence. *Geofluids*, *5*(3), 165–184. https://doi.org/10.1111/j.1468-8123.2005.00092.x
Newsom, H. E. (1980). Hydrothermal alteration of impact melt sheets with implications for Mars. *Icarus*, *44*(1), 207–216. https://doi.org/10.1016/0019-1035(80)90066-4
Ojha, L., Wilhelm, M. B., Murchie, S. L., Mcewen, A. S., Wray, J. J., Hanley, J., et al. (2015). Spectral evidence for hydrated salts in recurring slope lineae on Mars. *Nature Geoscience*. https://doi.org/10.1038/NGEO2546
Osinski, G. R. (2005). Hydrothermal activity associated with the Ries impact event, Germany. *Geofluids*, *5*(3), 202–220. https://doi.org/10.1111/j.1468-8123.2005.00119.x
Osinski, G. R., Tornabene, L. L., Banerjee, N. R., Cockell, C. S., Flemming, R., Izawa, M. R. M., et al. (2013). Impact-generated hydrothermal systems on Earth and Mars. *Icarus*, *224*(2), 347–363. https://doi.org/10.1016/j.icarus.2012.08.030
Pan, L., Ehlmann, B. L., Carter, J., & Ernst, C. M. (2017). The stratigraphy and history of Mars' northern lowlands through mineralogy of impact craters: A comprehensive survey. *Journal of Geophysical Research: Planets*, *122*, 1824–1854. https://doi.org/10.1002/2017JE005276
Parker, T. J., Stephen Saunders, R., & Schneeberger, D. M. (1989). Transitional morphology in West Deuteronilus Mensae, Mars: Implications for modification of the lowland/upland boundary. *Icarus*, *82*(1), 111–145. https://doi.org/10.1016/0019-1035(89)90027-4
Pelkey, S. M., Mustard, J. F., Murchie, S., Clancy, R. T., Wolff, M., Smith, M., et al. (2007). CRISM multispectral summary products: Parameterizing mineral diversity on Mars from reflectance. *Journal of Geophysical Research*, *112*, E08S14. https://doi.org/10.1029/2006JE002831
Plaut, J. J., Holt, J. W., Head, J. W., Gim, Y., Choudhary, P., Baker, D. M., et al. (2010). Thick ice deposits in Deuteronilus Mensae, Mars: Regional distribution from radar sounding, pp. 26–27.
Plaut, J. J., Safaeinili, A., Holt, J. W., Phillips, R. J., Head, J. W. III, Seu, R., et al. (2009). Radar evidence for ice in lobate debris aprons in the mid-northern latitudes of Mars. *Geophysical Research Letters*, *36*, L02203. https://doi.org/10.1029/2008GL036379
Rathbun, J. A., & Squyres, S. W. (2002). Hydrothermal systems associated with Martian impact craters. *Icarus*, *157*(2), 362–372. https://doi.org/10.1006/icar.2002.6838
Renne, P. R. (2013). Time scales of critical events around Cretaceous-Paleogene. *Boundary*, *339*(6120), 684–687. https://doi.org/10.1126/science.1230492
Robbins, S. J., & Hynek, B. M. (2011). Distant secondary craters from Lyot crater, Mars, and implications for surface ages of planetary bodies. *Geophysical Research Letters*, *38*, L05201. https://doi.org/10.1029/2010GL046450
Robbins, S. J., & Hynek, B. M. (2012a). A new global database of Mars impact craters ≥ 1 km: 1. Database creation, properties, and parameters. *117*, E05004. https://doi.org/10.1029/2011JE003966
Robbins, S. J., & Hynek, B. M. (2012b). A new global database of Mars impact craters ≥1 km: 2. Global crater properties and regional variations of the simple-to-complex transition diameter. *Journal of Geophysical Research*, *117*, E06001. https://doi.org/10.1029/2011JE003967
Robinson, D. (1987). Transition from diagenesis to metamorphism in extensional and collision settings. *Geology*, *15*(9), 866–869. https://doi.org/10.1130/0091-7613(1987)15
Robinson, D., Reverdatto, V. V., Bevins, R. E., Polyansky, O. P., & Sheplev, V. S. (1999). Thermal modeling of convergent and extensional tectonic settings for the development of low-grade metamorphism in the Welsh Basin. *Journal of Geophysical Research*, *104*, 2323–6979. https://doi.org/10.1029/1999JB900172
Ruff, S. W., & Christensen, P. R. (2001). Bright and dark regions on Mars: Particle size and mineralogical characteristics based on Thermal Emission Spectrometer data. *Journal of Geophysical Research*, *107*(E12). https://doi.org/10.1029/2001JE001580
Russell, P. S., & Head, J. W. (2002). The Martian hydrosphere/cryosphere system: Implications of the absence of hydrologic activity at Lyot crater. *Geophysical Research Letters*, *29*(17), 1827. https://doi.org/10.1029/2002GL015178.
Schiffman, P., & Day, H. W. (1999). Petrological methods for the study of very low-grade metabasites. In *Low-Grade Metamorphism* (pp. 108–142). Oxford, UK: Blackwell Publishing Ltd.
Schwenzer, S. P., Abramov, O., Allen, C. C., Clifford, S. M., Cockell, C. S., Filiberto, J., et al. (2012). Puncturing Mars: How impact craters interact with the Martian cryosphere. *Earth and Planetary Science Letters*, *335–336*, 9–17. https://doi.org/10.1016/j.epsl.2012.04.031
Schwenzer, S. P., & Kring, D. A. (2009). Impact-generated hydrothermal systems capable of forming phyllosilicates on Noachian Mars. *Geology*, *37*(12), 1091–1094. https://doi.org/10.1130/G30340A.1
Segura, T. L., McKay, C. P., & Toon, O. B. (2012). An impact-induced, stable, runaway climate on Mars. *Icarus*, *220*(1), 144–148. https://doi.org/10.1016/j.icarus.2012.04.013
Segura, T. L., Toon, O. B., & Colaprete, A. (2008). Modeling the environmental effects of moderate-sized impacts on Mars. *Journal of Geophysical Research*, *113*, E11007. https://doi.org/10.1029/2008JE003147
Squyres, S. W. (1978). Martian fretted terrain: Flow of erosional debris. *Icarus*, *34*(3), 600–613. https://doi.org/10.1016/0019-1035(78)90048-9
Stewart, S. T., & Valiant, G. J. (2006). Martian subsurface properties and crater formation processes inferred from fresh impact crater geometries. *Meteoritics & Planetary Science*, *41*(10), 1509–1537. https://doi.org/10.1111/j.1945-5100.2006.tb00433.x

Tanaka, K. L., Skinner, J. A., Dohm, J. M., Irwin, R. P., Kolb, E. J., Fortezzo, C. M., et al. (2014). Geologic map of Mars, U.S. Geol. Surv. Geol. Investig., 3292. https://doi.org/10.3133/sim3292

Toon, O. B., Segura, T., & Zahnle, K. (2010). The formation of Martian River valleys by impacts. *Annual Review of Earth and Planetary Sciences*, *38*(1), 303–322. https://doi.org/10.1146/annurev-earth-040809-152354

Tornabene, L. L., Osinski, G. R., McEwen, A. S., Wray, J. J., Craig, M. A., Sapers, H. M., & Christensen, P. R. (2013). An impact origin for hydrated silicates on Mars: A synthesis. *Journal of Geophysical Research: Planets*, *118*, 994–1012. https://doi.org/10.1002/jgre.20082

Tornabene, L. L., Watters, W. A., Osinski, G. R., Boyce, J. M., Harrison, T. N., Ling, V., & McEwen, A. S. (2018). A depth versus diameter scaling relationship for the best-preserved melt-bearing complex craters on Mars. *Icarus*, *299*, 68–83. https://doi.org/10.1016/j.icarus.2017.07.003

Turner, S. M. R., Bridges, J. C., Grebby, S., & Ehlmann, B. L. (2016). Hydrothermal activity recorded in post Noachian-aged impact craters on Mars. *Journal of Geophysical Research: Planets*, *121*, 608–625. https://doi.org/10.1002/2015JE004989

Velde, B., & Meunier, A. (2008). *The origin of clay minerals in soils and weathered rocks*. Berlin Heidelberg: Springer-Verlag. https://doi.org/10.1007/978-3-540-75634-7

Weiss, D. K., Head, J. W., Palumbo, A. M., & Cassanelli, J. P. (2017). Extensive Amazonian-aged fluvial channels on Mars: Evaluating the role of Lyot crater in their formation. *Geophysical Research Letters*, *44*, 5336–5344. https://doi.org/10.1002/2017GL073

Whitehead, J., Grieve, R. A. F., Garvin, J. B., & Spray, J. G. (2010). The effects of crater degradation and target differences on the morphologies of Martian complex craters. *GSA Special Papers*, *465*, 67–80. https://doi.org/10.1130/2010.2465(05)

Zolotov, M. Y., & Mironenko, M. V. (2007). Timing of acid weathering on Mars: A kinetic-thermodynamic assessment. *Journal of Geophysical Research*, *112*, E07006. https://doi.org/10.1029/2006JE002882